



1 Diurnal cycle of the semi-direct effect over marine stratocumulus in 2 large-eddy simulations

3
4 Ross J. Herbert¹, Nicolas Bellouin¹, Ellie J. Highwood¹, Adrian A. Hill²

5 ¹Department of Meteorology, University of Reading, Reading, RG6 6BB, UK

6 ²Met Office, Fitzroy Road, Exeter, EX1 3PB, UK

7 *Correspondence to:* Ross Herbert (r.j.herbert@reading.ac.uk)

8 The rapid adjustment, or semi-direct effect, of marine stratocumulus clouds to elevated layers of absorbing aerosols may
9 enhance or dampen the radiative effect of aerosol-radiation interactions. Here we use large eddy simulations to investigate the
10 sensitivity of stratocumulus clouds to the properties of an absorbing aerosol layer located above the inversion layer. The sign
11 of the daily mean semi-direct effect depends on the properties of the aerosol layer, the properties of the boundary layer, and
12 the model setup. Diurnal variations in the cloud response mean that an instantaneous semi-direct effect is unrepresentative of
13 the daily mean, and that observational studies may under- or over-estimate semi-direct effects depending on the observed
14 time of day. The observed role of the distance between the cloud top and the absorbing layer in modulating the strength of the
15 cloud and radiative response is reproduced by the large eddy simulations. Both cloud response and semi-direct effect increase
16 for thinner, denser, layers of absorbing aerosol located nearer the cloud layer. The cloud response is particularly sensitive to
17 the mixing state of the boundary layer: well-mixed boundary layers generally result in a negative daily mean semi-direct effect,
18 and poorly mixed boundary layers result in a positive daily mean semi-direct effect. Properties of the boundary layer and
19 model setup, particularly the sea surface temperature, precipitation, and properties of the air entrained from the free
20 troposphere, also impact the magnitude of the semi-direct effect and the timescale of adjustment. These results suggest that
21 the semi-direct effect simulated by coarse-resolution models may be erroneous because the cloud response is sensitive to
22 small-scale processes, especially the sources and sinks of buoyancy.

23 1 Introduction

24 Semi-permanent decks of marine stratocumulus clouds represent an important negative radiative effect within the Earth's
25 energy budget (Hartmann et al., 1992; Hartmann and Short, 1980; Wood, 2012). In addition, the sharp inversion layer and
26 small-scale turbulent processes that characterise the formation and maintenance of these clouds represent considerable
27 uncertainty in climate models, so stratocumulus clouds remain a key uncertainty in future climate projections (Bony and
28 Dufresne, 2005; Klein et al., 2017; Wood, 2012). Marine stratocumulus clouds are sensitive to sea surface temperature (SST)
29 and large-scale atmospheric properties both above the inversion, like subsidence rate and thermodynamic properties of the



30 overlying air mass, and below the inversion, like cloud condensation nuclei sinks and sources, that impact turbulent processes
31 and dynamics throughout the boundary layer (e.g., Bretherton et al., 2013; Feingold et al., 2010; Sandu et al., 2010). Therefore,
32 small changes to these properties could result in large changes to the fluxes of radiation in the atmosphere.

33

34 Perturbations to the aerosol distribution result in a radiative forcing through both aerosol–radiation and aerosol–cloud
35 interactions; this distinction separates the radiative forcing caused by aerosol scattering and absorption of longwave and
36 shortwave radiation from that caused by the availability of cloud condensation nuclei. Aerosol–cloud interactions lead to
37 changes in cloud albedo and subsequent rapid adjustments to the cloud properties that include changes to precipitation and
38 cloud evolution (Sherwood et al., 2015). Aerosol–radiation interactions result in instantaneous changes to the extinction profile
39 (also referred to as the direct radiative effect) and therefore heating profile, which lead to rapid adjustments in the physical and
40 radiative properties of the cloud (referred to in this paper as the semi–direct effect, SDE, for convenience). Quantifying rapid
41 adjustments is important as they may act to dampen or strengthen the instantaneous forcing. Aerosol–radiation interactions
42 represent an important uncertainty in the anthropogenic radiative forcing of the climate over the industrial era, especially from
43 absorbing aerosol species such as black carbon which may result in pronounced semi–direct effects (Boucher et al., 2013). In
44 a recent climate model intercomparison study Stjern et al. (2017) found that a ten–fold increase in black carbon emissions
45 resulted in a strong positive direct effect which was partially offset by a negative SDE. Although all models agree on the sign
46 (negative) they disagree on the size of that offset, from 12 to 63 % for the models studied by Stjern et al. (2017). High–
47 resolution models that can sufficiently represent the dominant processes within the boundary layer and cloud are a powerful
48 benchmark to test the realism of the response simulated by the climate–scale models.

49

50 During the African dry season, which lasts from August to October, plumes of strongly absorbing biomass burning aerosol
51 from central Africa are transported westward over the semi–permanent marine stratocumulus deck of the Southeast Atlantic
52 Ocean, where they eventually subside and mix into the boundary layer (Das et al., 2017). Observational and modelling studies
53 suggest that elevated absorbing layers result in thicker clouds and a negative SDE (Adebisi and Zuidema, 2018; Johnson et
54 al., 2004; Wilcox, 2010), and may impact the stratocumulus–to–cumulus transition process (Yamaguchi et al., 2015; Zhou et
55 al., 2017). Once mixed into the cloud layer the absorbing aerosol exerts aerosol–radiation interactions that enhance cloud
56 evaporation (Hill and Dobbie, 2008; Johnson et al., 2004) and aerosol–cloud interactions that impact microphysical and
57 dynamical processes (e.g., Feingold et al., 2010; Gordon et al., 2018; Hill et al., 2009). Observational studies have used satellite
58 retrievals from the NASA A–Train to investigate the interaction between clouds and absorbing aerosol over the Southeast
59 Atlantic. Wilcox (2010) used co–located CALIPSO, OMI, and AMSR–E retrievals and found that for all overcast scenes liquid
60 water path (LWP) increased for high aerosol loading. This response was attributed to absorbing aerosol layers above the cloud
61 top enhancing the heating rate and decreasing entrainment across the inversion. However, satellites do not provide direct
62 observations of entrainment and an alternative explanation could be that the aerosol layers travel in relatively moist layers
63 (Adebisi et al., 2015), increasing moisture transport across the inversion layer, even if entrainment remained unchanged. In a



64 study with a similar methodology, Costantino and Bréon (2013) separated the CALIPSO-derived aerosol layer heights into
65 cases when the smoke was close to (< 100 m) and well-separated (< 750 m) from the cloud top. The authors found that when
66 the aerosol layers are well separated from cloud top the LWP and cloud optical thickness showed no statistically significant
67 dependence on aerosol loading. These results are supported by Adebisi and Zuidema (2018) who used satellite observations
68 and reanalysis products to show evidence that the sensitivity of low-cloud cover to elevated aerosol layers increased for small
69 cloud-aerosol gaps. These observations suggest that the distance between the elevated aerosol layer and cloud layer plays an
70 important role in the strength of the SDE. Additionally, a recent satellite study of cloud-aerosol gaps by Rajapakshe et al.
71 (2017) suggests that the elevated aerosol layers may be closer to the cloud than previously thought, which demonstrates that
72 elevated layers may have an even more important impact on the clouds.

73

74 The observations hint at the potential importance of the extent of cloud-aerosol gap for the SDE. However, this complexity is
75 not reflected in the frameworks presented in current reviews (Bond et al., 2013; Koch and Del Genio, 2010), and there is a
76 lack of high-resolution modelling studies investigating the SDE from elevated layers of absorbing aerosol. Johnson et al.
77 (2004) used large-eddy simulation (LES) to investigate the semi-direct of absorbing aerosols on non-precipitating marine
78 stratocumulus. In an experiment where a ~ 1 km thick layer of absorbing aerosol, with an aerosol optical depth (AOD) of 0.2
79 at 550 nm, was present above the marine boundary layer throughout a 48-hr simulation, the absorbing aerosol enhanced the
80 temperature inversion at the top of the boundary layer, weakening the entrainment rate across the inversion, and producing a
81 shallower, moister boundary layer and a higher LWP. The 48-hr mean SDE was estimated to be -9.5 Wm^{-2} , almost entirely
82 cancelling a direct effect of $+10.2 \text{ Wm}^{-2}$. Yamaguchi et al. (2015) and Zhou et al. (2017) used LES models to investigate the
83 transition of marine stratocumulus to cumulus in the presence of a smoke layer. As the marine boundary layer deepened, the
84 cloud-aerosol gap decreased until the smoke layer made contact with the cloud layer. Both studies found little LWP response
85 when the smoke layer was separated by a no-aerosol gap. Yamaguchi et al. (2015) found that the elevated smoke layer reduced
86 boundary layer turbulence and cloud cover through a decrease in longwave cloud-top cooling. By isolating the aerosol heating
87 above and below the boundary layer top Zhou et al. (2017) found that when the layer was directly above the inversion layer
88 the elevated aerosol layer strengthened the inversion, inhibiting entrainment, and increased LWP and cloud cover, resulting in
89 a negative SDE. Global models have also been used to investigate the radiative impact of biomass burning aerosol in
90 stratocumulus regions (e.g., Lu et al., 2018; Penner et al., 2003; Sakaeda et al., 2011), however, Das et al. (2017) show that
91 these coarser resolution models may be unable to reproduce the observed vertical distribution of absorbing aerosol layers over
92 the southeast Atlantic, resulting in an under-representation of elevated aerosol layers and increased uncertainty in their
93 radiative impact.

94

95 In summary, observation and modelling studies suggest that the diurnal cycle and evolution of marine stratocumulus are
96 strongly impacted by the presence of absorbing aerosol layers at and above the top of the boundary layer. The SDE may act to
97 counteract or enhance the direct effect, resulting in either a small or large net radiative effect from aerosol-radiation



98 interactions. Yet the sensitivity of the SDE to the properties of the elevated aerosol layer has not been fully investigated. In
99 this study the UK Met Office Large Eddy Model (LEM) is used to investigate and quantify the impact that the properties of
100 an elevated absorbing aerosol layer have on the cloud and radiative response of marine stratocumulus. Section 2 presents the
101 LEM and its configuration and introduces a set of experiments designed to assess the SDE and its sensitivity to the aerosol
102 layer properties. Section 3 focuses on a single experiment to understand the processes that drive the cloud response and SDE,
103 then assesses the sensitivity of this response to the aerosol layer properties. Section 3 also investigates the robustness of that
104 assessment to the processes that affect the maintenance of the cloud, namely precipitation, sea surface temperature, and
105 boundary layer depth. Section 4 summarises the results, comparing to other modelling studies and observations, and discussing
106 the limitations of this study and identifying remaining questions.

107 2 Model description and setup

108 2.1 Description of model

109 The LEM (Gray et al., 2001) is a non-hydrostatic high-resolution numerical model that explicitly resolves the large-scale
110 turbulent motions responsible for the energy transport and flow. Sub-grid scale turbulence responsible for the dissipation of
111 kinetic energy is parameterised. Prognostic variables are the three-dimensional velocity fields (u, v, w), liquid-water potential
112 temperature (θ_l), and mass-mixing ratios of water vapour (q_v), liquid water (q_l), and rain (q_r). Liquid water mass is prognosed
113 at every grid point using a condensation–evaporation scheme in which excess supersaturation is converted to liquid water and
114 vice versa for sub-saturated air. Warm rain processes are represented by a single-moment microphysics scheme that includes
115 autoconversion and cloud droplet collection following Lee (1989), sedimentation of rain, and evaporation of rain into dry air.
116 The influence of aerosol on cloud droplet number concentration is not included in this study and cloud droplet number is fixed
117 to 240 cm^{-3} for microphysical processes. Surface fluxes are calculated using Monin–Obukhov similarity theory (Monin and
118 Obukhov, 1954) with a prescribed constant sea surface temperature. A damping layer that relaxes all prognostic variables to
119 their horizontal mean is present above an altitude of 775 m (~ 150 m above the cloud layer; see Sect. 2.2) with a height scale
120 of 650 m and a timescale of 30 s. This prevents the reflection of gravity waves at the rigid top boundary and prevents the
121 production of trapped buoyancy waves above the inversion layer (Ackerman et al., 2009). The subsidence rate w_s is represented
122 by a height dependent function $w_s(z) = -Dz$ for which large-scale divergence (D) is prescribed. The model is run with a variable
123 time step with a maximum of 0.5 seconds. The LEM radiation scheme, described by Edwards and Slingo (1996), is a two-
124 stream solver with six shortwave spectral bands and eight longwave bands that calculates the vertical distribution of radiative
125 fluxes and heating rates. The scheme includes six aerosol species with wavelength and humidity-dependent mass absorption
126 coefficients, mass scattering coefficients, and asymmetry factors. A single value for the mean cloud droplet effective radius of
127 $10 \mu\text{m}$ is prescribed in the radiation scheme.



128 2.2 Model setup

129 All simulations are three dimensional. The model domain is 5200 m in the horizontal with a horizontal grid resolution of 40 m,
130 and 2600 m in the vertical with a variable vertical grid resolution with ~6 m resolution at the cloud top and inversion and less
131 than 10 m throughout the boundary layer (BL). The LEM is configured here to produce a stratocumulus with a consistent
132 diurnal cycle over an 8-day timescale. The initial profiles of θ_i and q_i were taken from Johnson et al. (2004) and based on
133 subtropical marine stratocumulus observations from the First International Satellite Cloud Climatology Project Regional
134 Experiment (FIRE) (Hignett, 1991) in the subtropical Pacific Ocean. A series of 10-day simulations without absorbing aerosol
135 were run with varying subsidence rates to obtain steady-state profiles of θ_i and q_i that would produce a consistent stratocumulus
136 layer with a maximum cloud top height of 600 m. The resulting initialisation profiles are shown in Table 1; the BL is 0.6 g kg^{-1}
137 drier than in Johnson et al. (2004) and Hill et al. (2008) due to the inclusion of precipitation in our study and a cooler SST,
138 which was necessary in order to attain a similar cloud LWP to these studies. The large-scale divergence D is set to $5.5 \times 10^{-6} \text{ s}^{-1}$,
139 giving a subsidence rate of $w_s = -3.3 \text{ mm s}^{-1}$ at the cloud top. D and w_s are within the observed range for marine stratocumulus
140 regions (Zhang et al., 2009) and of similar magnitude to other stratocumulus LES studies (e.g., Johnson et al., 2004; De Roode
141 et al., 2014). The initial profiles describe a well-mixed moist BL capped by a sharp (10 K) inversion at 600 m with a warm
142 and dry free troposphere (FT) above the inversion. To account for a source of large-scale heat divergence a cooling rate of
143 0.1 K day^{-1} is applied. This value is lower than the 1.0 K day^{-1} used by Johnson et al. (2004) and Hill et al. (2008) because the
144 greater cooling rates result in an unstable cloud top height in our simulations which is undesirable as we require a consistent
145 cloud layer to isolate the cloud response due to the absorbing aerosol. A prescribed surface pressure of 1012.5 hPa is used, and
146 zonal and meridional geostrophic winds are 6.0 m s^{-1} and -1.0 m s^{-1} , respectively. The radiation scheme is set up for consistency
147 with the FIRE campaign with a time-varying solar zenith angle for mid-July at the co-ordinates 33°N , 123°W . Radiation
148 calculations are performed every 30 seconds. Surface roughness is fixed at $2 \times 10^{-4} \text{ m}$ and SST at 287.2 K .

149

150 **Table 1. Initial profiles used in the control simulations**

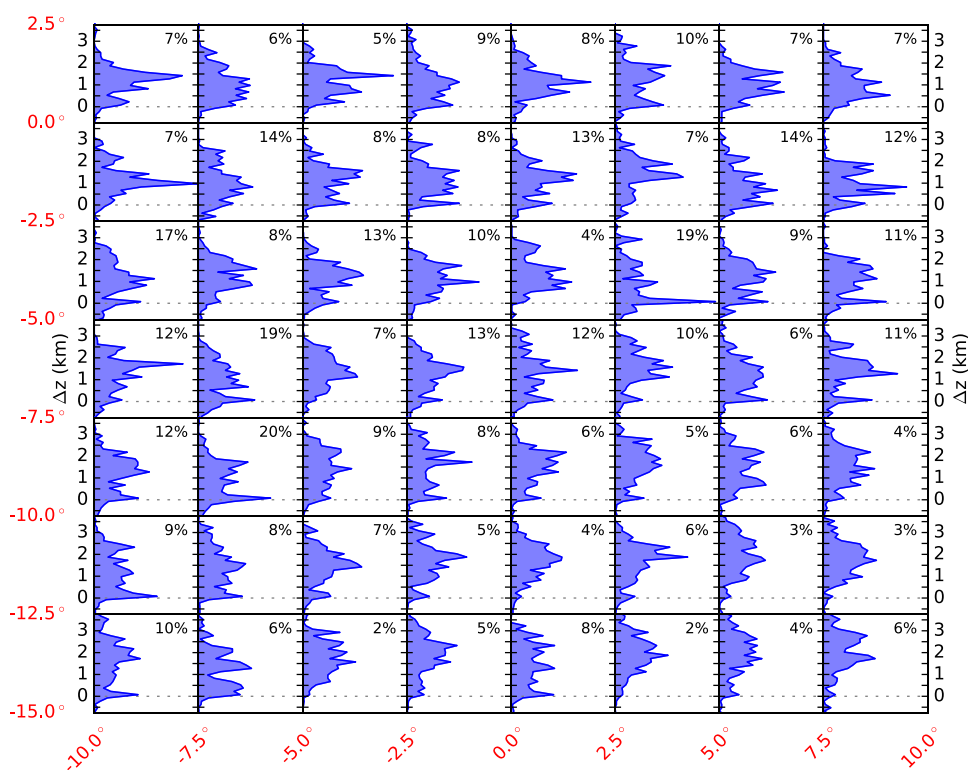
Altitude (m)	Liquid-water potential temperature (K)	Total water mixing ratio (g kg^{-1})
0	287.5	9.0
600	287.5	9.0
601	297.0	5.5
750	300.0	5.5
1000	301.7	5.5
1500	303.2	5.5
2600	304.0	5.5

151



152 2.3 Setup of elevated-aerosol experiments

153 To simulate the effect of an elevated absorbing-aerosol layer above the cloud top, a layer of dry aerosol is prescribed,
154 consisting of soot-like and water-soluble-like aerosol, representing predominantly absorbing and scattering species,
155 respectively. The interaction of longwave and shortwave radiation with the aerosol layer results in localised heating rates that
156 are coupled to the LEM. The prescribed aerosol layer properties include the height of layer base above the inversion layer
157 (referred to as the cloud-aerosol gap), geometric thickness, mean single-scattering albedo (SSA), and AOD. These properties
158 are set at the beginning of the experiment and applied during each call to the radiation scheme. Using the prescribed geometric
159 thickness of the aerosol layer, a balance between the mass-mixing-ratio of soot and water-soluble aerosol is used to achieve
160 the desired SSA and AOD throughout the simulation (see Appendix for more details on the method employed). In these
161 experiments SSA is 0.9, which is towards the higher end of the range of SSA for biomass burning aerosol (Peers et al., 2016)
162 and thus represents a relatively conservative value for the absorption of the aerosol layer.



163

164 **Figure 1. Normalised frequency of occurrence of gap distance between cloud layer top and aerosol base heights from CALIOP for**
165 **single layer coincidences of aerosol and cloud in the months of July, August, and September 2007–2016 over the southeast Atlantic**
166 **(15°S to 2.5°N, 10°W to 10°E). Layer heights are binned from -1.5 to 5.5 km in 150 m increments and data in each grid has been**
167 **normalised to the maximum frequency across the whole study area. The percentage of scenes where the aerosol layer base is below**
168 **the cloud top height is shown in the top right of each subplot.**



169

170 Realistic cloud–aerosol gaps are needed for the elevated–aerosol experiments. They are taken from observations from the
171 CALIPSO Cloud–Aerosol Lidar with Orthogonal Polarization (CALIOP) instrument (5-km resolution, 532 nm Aerosol Layer
172 Product and Cloud Layer Product, v4.10, level 2 data) over the Southeast Atlantic Ocean (15°S to 2.5°N, 10°W to 10°E). The
173 distance Δz between the retrieved cloud top and the aerosol base heights is determined from scenes where vertical profiles only
174 include a single layer of low cloud and a single layer of aerosol. Figure 1 shows the normalised frequency of occurrence of Δz
175 in 2.5-degree grids for all scenes within July, August, and September between 2007 and 2016. For the majority of scenes, the
176 layer of aerosol tends to be above, or directly above, the cloud top layer. There is considerable variation in Δz at all locations;
177 to the north of the study area the peak Δz is ~ 1 km, whereas to the south of the study area the peak Δz is closer to 2 km. In
178 many regions there is a high frequency of the aerosol layer being in close proximity to the cloud top. Rajapakshe et al. (2017)
179 have shown that in the southeast Atlantic the CALIOP product overestimates the aerosol layer base height and layers are likely
180 much closer to the cloud layer than previously thought; they find that in 60% of their above–cloud–aerosol cases the absorbing
181 layer is less than 360 m above the cloud deck, therefore our Δz is likely overestimated.

182

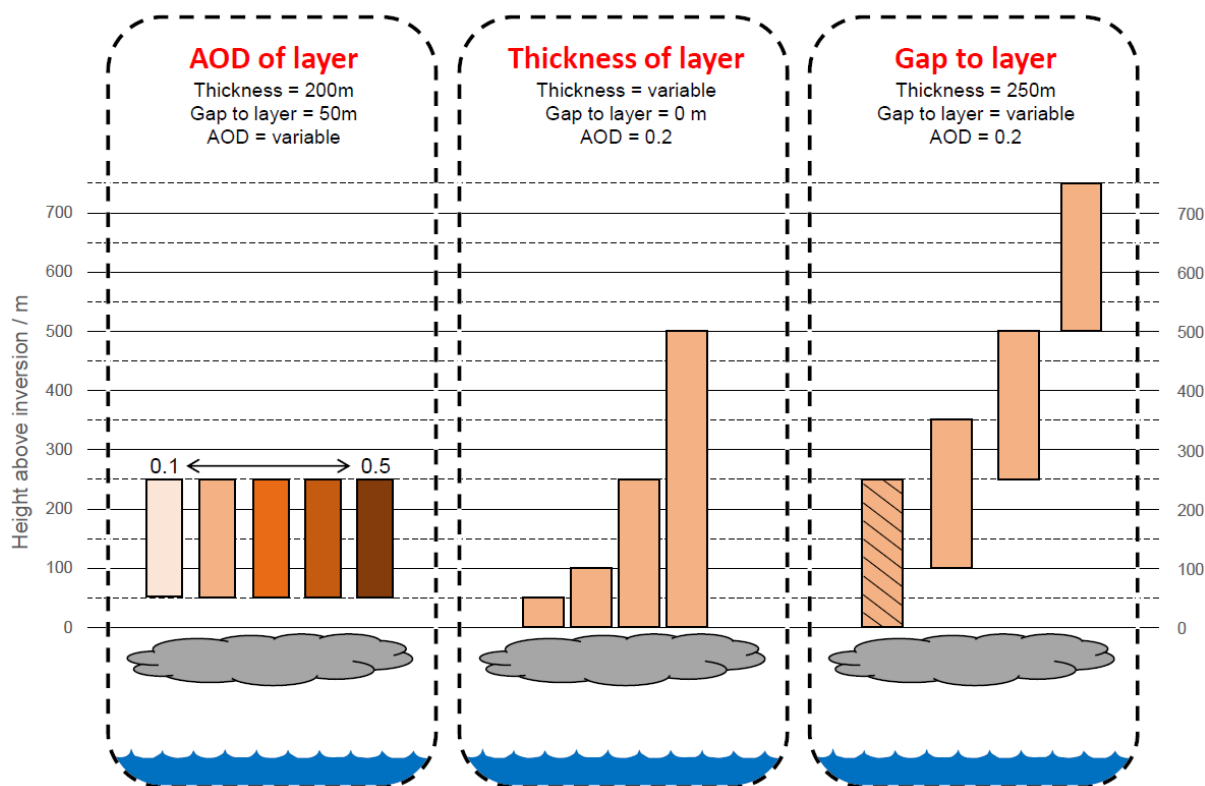
183 The CALIOP analysis (Fig. 1) suggests that elevated aerosol layers predominantly exist within 1500 m of the cloud top with
184 a common occurrence of layers in close proximity (< 150 m) to the cloud, and the study by Rajapakshe et al. (2017) suggests
185 the aerosol layers are predominantly within 360 m of the cloud top. In-line with this we focus on layers of absorbing layers
186 that range from directly above the cloud layer ($\Delta z = 0$ m) to elevated layers at $\Delta z = 500$ m, and we additionally examine the
187 role of the aerosol layer depth which, for a given AOD, will impact the vertical distribution and strength of the localised heat
188 perturbation.

189

190 A schematic of the experiments designed to investigate the sensitivity of the SDE and cloud diurnal cycle to key layer
191 properties, namely the AOD, geometric thickness, and the cloud–aerosol gap, is shown in Fig. 2. The first set investigates the
192 sensitivity of the SDE to the strength of the aerosol layer absorption. Following AOD observations by Chand et al. (2009), the
193 AOD of the layer is varied from 0.1 to 0.5 while keeping the geometric thickness constant at 200 m and the cloud–aerosol gap
194 at 50 m. The second set of experiments investigates the sensitivity of the cloud response to the geometric thickness of the
195 aerosol layer at constant AOD. This type of experiment is analogous to a satellite retrieval that estimates the AOD and aerosol
196 layer top but does not detect the lower extent of the aerosol layer. This is a known deficiency with retrievals made using
197 wavelengths that are strongly attenuated by biomass burning aerosol such as the 532 nm channel currently used in the
198 CALIPSO aerosol products (Rajapakshe et al., 2017). For these experiments the geometric thickness of the aerosol layer is
199 increased from 50 to 500 m with no cloud–aerosol gap and are effectively experiments with variable density of aerosol
200 particles, since with a fixed AOD the aerosol layer mass–mixing ratio decreases with increasing geometric thickness of the
201 layer. The final set of experiments investigates the impact of the cloud–aerosol gap by placing the aerosol layer from 0 to
202 500 m above the inversion layer while keeping geometric thickness and AOD constant. A full list of experiments performed



203 is presented in Table 2. We use one of the experiments, referred to as the base experiment, to provide an initial in-depth analysis
 204 of the cloud and radiative response. In the base experiment (hatched experiment in Fig. 2) a 250 m thick absorbing aerosol
 205 layer with an AOD of 0.2 is placed directly above the inversion layer.
 206



207
 208 **Figure 2. Schematic showing the experiments performed for the aerosol-sensitivity simulations. The hatched experiment is named**
 209 **the base experiment and is used to provide initial analysis of the semi-direct effect in Sect. 3.2. AOD stands for aerosol optical depth**
 210 **and is given at a mid-band wavelength of 505 nm.**

211
 212 The SDE is calculated as a residual of the difference in top-of-atmosphere net radiation (F_{TOA}) between the aerosol and no-
 213 aerosol simulations, minus the direct radiative effect (DRE):

214

$$SDE = (F_{TOA, no-aerosol} - F_{TOA, aerosol}) - DRE \quad (1)$$

215
 216 where F_{TOA} is calculated using the upward (\uparrow) and downward (\downarrow) fluxes of longwave (LW) and shortwave (SW) radiation:

217

$$F_{TOA} = F_{TOA, SW}^{\downarrow} - (F_{TOA, SW}^{\uparrow} + F_{TOA, LW}^{\uparrow}) \quad (2)$$



218

219 DRE is calculated as the difference between F_{TOA} and that obtained in a second, diagnostic, call to the radiation scheme with
220 the same profiles of liquid water, water vapour, and atmospheric gases, but without aerosol.

221

222 **Table 2. Breakdown of all experiments performed. AOD stands for aerosol optical depth and is given at a mid-band wavelength of**
223 **505 nm.**

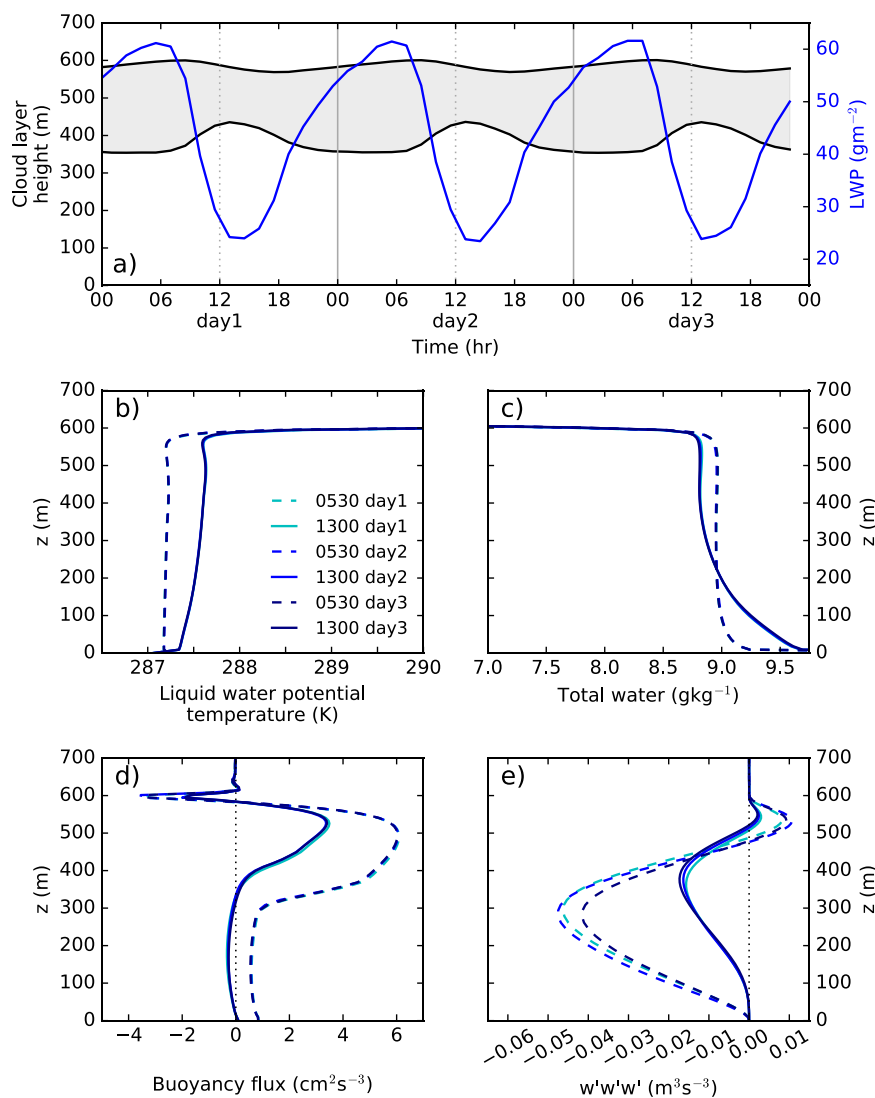
Type of experiment	Layer properties		
	Cloud–aerosol gap (m)	Layer thickness (m)	Layer AOD
Variable AOD	50	200	0.1
	50	200	0.2
	50	200	0.3
	50	200	0.4
	50	200	0.5
Variable thickness	0	50	0.2
	0	100	0.2
	0	250	0.2
	0	500	0.2
Variable gap	0*	250	0.2
	100	250	0.2
	250	250	0.2
	500	250	0.2

* Base experiment used for initial analysis

224 3 Results

225 3.1 No-aerosol experiment

226 The no-aerosol experiment is initialised then run for fifteen days without the presence of an aerosol layer. The first five days
227 are used as a spin-up period that allows the BL to reach a steady state; the following three days (days 6, 7, and 8 of the
228 simulation) are shown in Fig. 3.



229

230 **Figure 3. Evolution of domain averaged cloud properties in the no-aerosol simulation including: a) cloud top and base (black lines;**
 231 **left axis), and liquid water path (blue line; right axis); and vertical profiles taken at 0530 (dashed lines) and 1300 (solid lines) on each**
 232 **day for b) liquid water potential temperature, c) total water mass mixing ratio, d) buoyancy flux, and e) the perturbation in mean**
 233 **vertical velocity $w'w'w'$.**

234 The no-aerosol experiment produces a cloud-topped BL with strong diurnal variations. During the daytime, cloud top height
 235 decreases and cloud base height increases, thinning the cloud and producing a diurnal cycle of LWP that reaches a maximum
 236 of 60 g m^{-2} at dawn and a minimum of 25 g m^{-2} just after midday (Fig. 3a). The diurnal cycle can be separated into a growth
 237 phase between 1400 and 0600, and a decay phase between 0700 and 1300. The growth phase is driven by pronounced buoyancy
 238 production during the night (Fig. 3d) from longwave cloud-top cooling and evaporative cooling of entrained air, which drives
 239 strong eddies below cloud (Fig. 3e). During the daytime, solar heating reduces cloud-top negative buoyancy through an offset



240 in the longwave cooling and reduces surface-driven positive buoyancy through weakened surface-to-atmosphere gradients.
241 This weakens the BL circulation and prevents mixing throughout the BL and promotes a decoupled state in which the flux of
242 moisture from the surface to the cloud is insufficient to maintain the cloud base height, as evident from the non-constant BL
243 profiles of θ_l (Fig. 3b) and q_l (Fig. 3c) at 1300 hours. The weakened flux and solar heating of the cloud drives the lifting
244 condensation level upwards and causes the cloud base to increase with height, producing the decay phase. During the daytime
245 weakened BL eddies are unable to ‘push’ against the subsidence at the BL top, which decreases the BL depth and cloud top
246 height. Due to the different processes that control the cloud top and cloud base diurnal variations, the cloud top height minimum
247 occurs about 2 hours after the cloud base reaches its maximum. The cloud layer, LWP and thermodynamic profiles in Fig. 3
248 (a – e) show very little change over the three days of the simulation and present a stratocumulus deck with a consistent diurnal
249 cycle in a steady state. This provides a suitable simulation to use as control for the elevated-aerosol experiments.

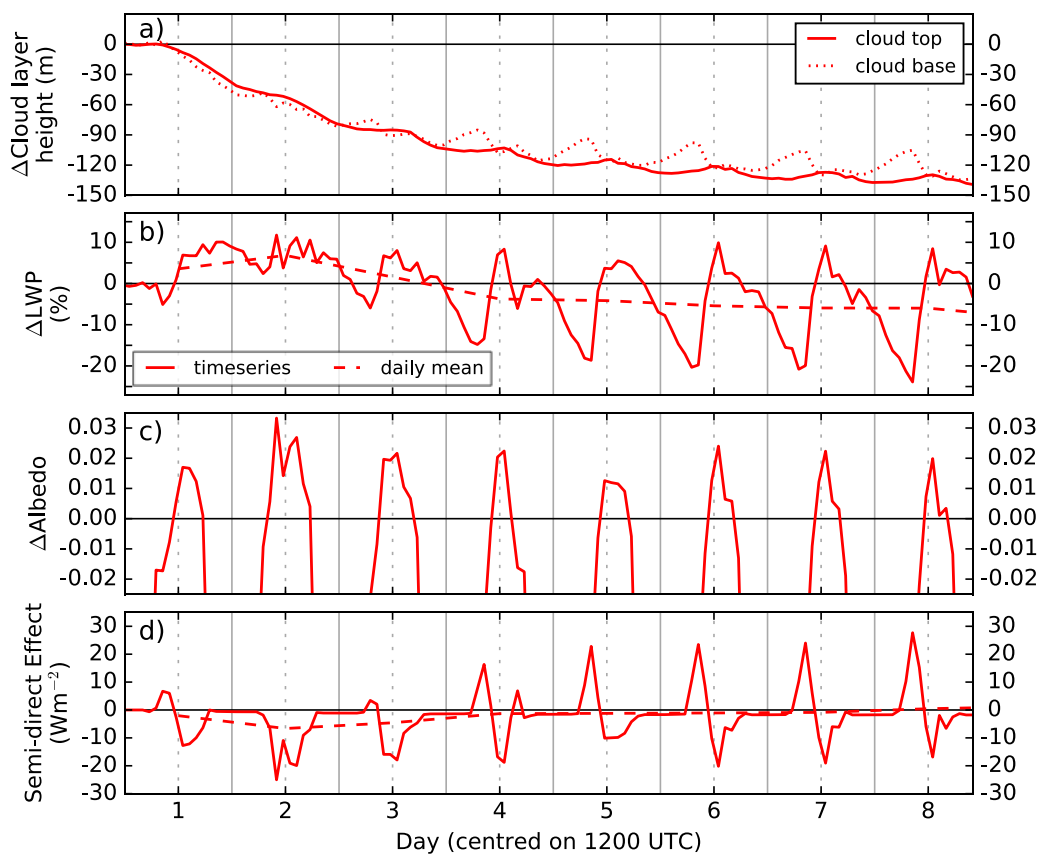
250 3.2 Cloud response to elevated aerosol layer in the base experiment

251 We begin with the base experiment (hatched experiment in Fig. 2) where a 250 m thick absorbing aerosol layer with an AOD
252 of 0.2 is placed directly above the inversion layer. Following a five-day spin-up period without aerosol, the simulation runs
253 for a further ten days with the aerosol layer present. The domain-averaged cloud response following the introduction of aerosol
254 is shown in Fig. 4 and compared to the no-aerosol simulation.

255
256 The simulations show that the absorbing aerosol drives changes in the diurnal cycle of cloud depth and LWP, predominantly
257 through changes in the cloud base height. The presence of the absorbing aerosol drives a decrease in cloud top height (Fig. 4a)
258 which occurs predominantly in the afternoon and evening and is indicative of a decrease in entrainment across the inversion
259 layer. During the initial two days the cloud base (Fig. 4a) decreases in altitude ~ 10 m more than the cloud top resulting in a
260 thicker cloud, however from day three onwards there is less growth of the cloud throughout the evening and early morning,
261 followed by less thinning throughout the day. Compared to the cloud in the presence of no aerosol, the introduction of the
262 absorbing aerosol layer results in relatively less LWP (Fig. 4b) during the growth phase of the cloud and more LWP during
263 the decay phase.

264
265 The SDE (Fig. 4d) has a strong diurnal cycle that is directly driven by modifications to the cloud albedo diurnal cycle (Fig.
266 4c) and shows considerable sensitivity to the LWP response during the cloud decay phase around midday. In the first three
267 days the albedo response is positive from mid-morning to the late afternoon. This drives an overall negative daily mean SDE.
268 The length of time with a positive albedo response gets shorter as the simulation progresses, driving an increasingly positive
269 SDE in the morning that cancels out, on a daily mean, the negative SDE in the afternoon. Consequently, the daily mean SDE
270 is negative for the initial three days but almost net zero SDE from the fourth day onwards.

271



272

273 **Figure 4.** 10-day timeseries of domain-averaged cloud response to a layer of aerosol directly above the boundary layer inversion
274 with an aerosol optical depth of 0.2 and geometric thickness of 250 m. Plots show the response from a) cloud top height (solid line)
275 and cloud base height (dotted line), b) cloud liquid water path (LWP), c) albedo, and d) the semi-direct effect. Solid lines in b), c),
276 and d) show the timeseries of the response and dashed lines in b) and d) show the daily mean.

277

278 The cloud response and SDE are therefore markedly different in the initial phase compared to the steady-state that is reached
279 after 6 or 7 days following the introduction of the absorbing aerosol layer. In that steady-state phase the BL depth has decreased
280 by ~130 m (~20%) and the diurnal cycle response in cloud thickness has stabilised. This suggests there are timescales in the
281 response to the introduction of the aerosol layer: a short-term response that can be interpreted as a rapid adjustment of the
282 humidity profile, and longer-term response that can be interpreted as a new equilibrium state for the BL sources of moisture,
283 turbulence, and heat.

284



285 This study focuses on the initial response because it is more relevant for real–world understanding as the aerosol perturbation
286 is unlikely to remain constant for several days, and the lifetime of stratocumulus decks is generally on the order of a few days
287 only. However, the steady–state response provides insight into the key drivers behind the BL modifications.

288 3.2.1 Initial response in the base experiment

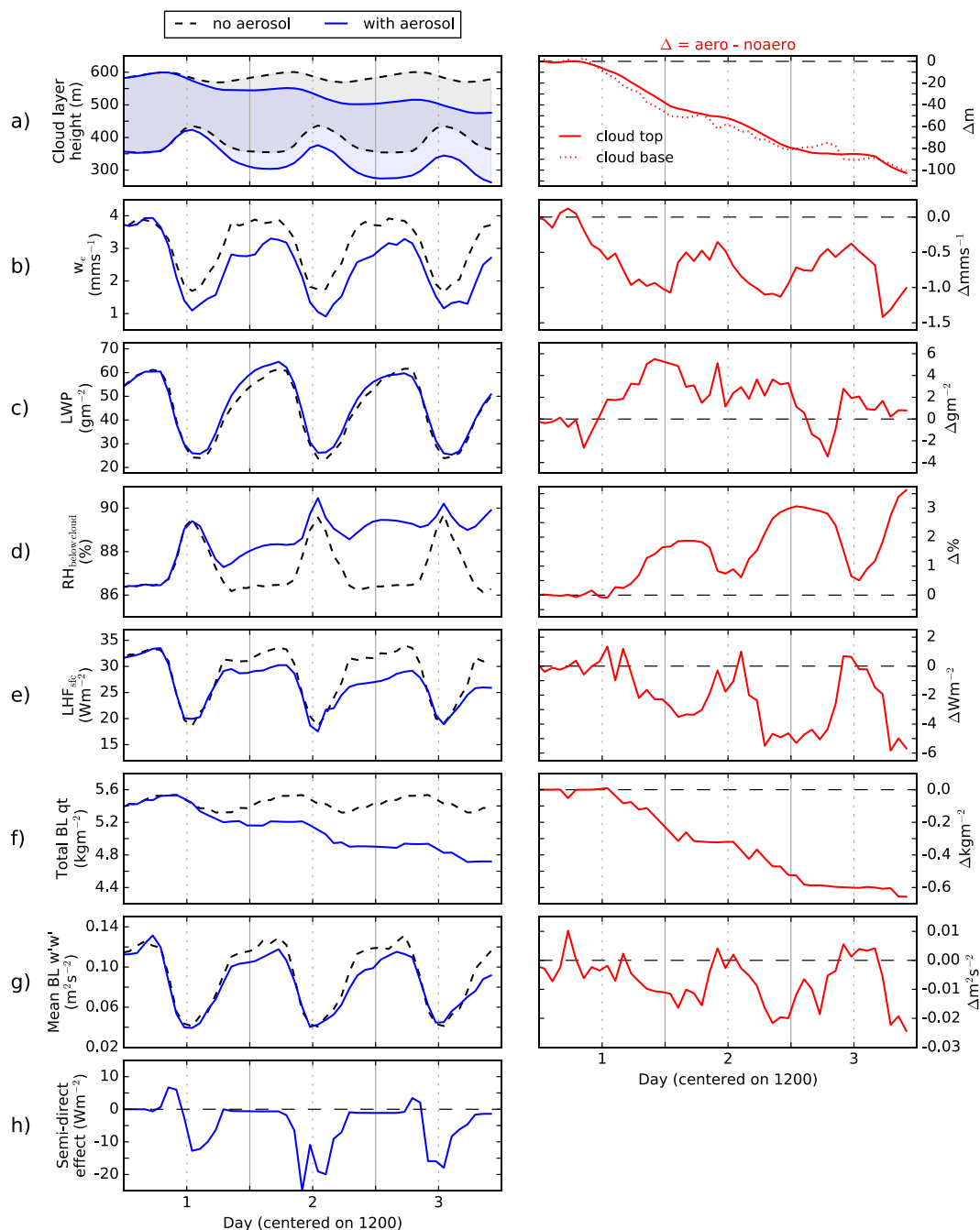
289 The domain–averaged timeseries of the response in the first three days following the introduction of the aerosol layer (days 6,
290 7, and 8 of the simulation) are shown in Fig. 5. The initial response of the cloud to the elevated aerosol layer is driven by the
291 weakening of the entrainment rate ($w_e = dz_{\text{cloudtop}} / dt - w_s$) and subsequent increase in the RH below cloud which acts to
292 produce a thicker cloud in the first two days. Solar radiation heats the elevated absorbing aerosol layer above the inversion
293 layer. Strengthening of the temperature inversion at the top of the BL drives a weakened w_e (Fig. 5b) which causes the BL
294 depth to decrease (Fig. 5a). Simultaneously, there is an increase in RH below cloud (Fig. 5d), which allows the cloud base
295 height to decrease (Fig. 5a) and the LWP to increase (Fig. 5c); this response continues for the first two days, after which the
296 LWP starts to display a diurnal response with a decrease in LWP during the night and an increase in the afternoon. The increase
297 in RH occurs due to the weakened w_e which reduces the amount of warm dry FT air that is mixed into the BL and allows the
298 cloud layer to maintain a higher RH.

299

300 The thinner cloud on the morning of the third day is driven by changes to the supply of moisture to the cloud layer. The
301 enhanced RH below cloud (caused by an increase in water vapour) and weakened vertical motions (Fig. 5g) drive a strong
302 reduction in surface evaporation as demonstrated by the decrease in latent heat flux (LHF; Fig. 5e), especially during the night.
303 By the end of day three the LHF at the surface has reduced by 20% and the total column water content (Fig. 5f) has reduced
304 by 10%. During the night when the BL is well mixed this reduction in total water content prevents the cloud from developing
305 to the same extent as in the no–aerosol simulation, resulting in a thinner cloud when the sun rises. This process is amplified by
306 the reduced BL dynamics which will weaken the flux of moisture from the sub–cloud region to the cloud.

307

308 The thicker cloud on the afternoon of the third day is driven by relatively stronger coupling with the surface moisture fluxes
309 at midday, which produces a slightly thicker cloud and a negative SDE (Fig. 5h). Under no–aerosol conditions, shortwave
310 absorption by the cloud stabilises the cloud layer during the day, which results in a degree of decoupling between the surface
311 layer and cloud base (Fig. 3). When an elevated absorbing aerosol layer is present, the decrease in cloud layer height, following
312 the BL depth decrease, allows better coupling to the surface, which becomes increasingly important around midday when BL
313 dynamics are weakest (Fig. 5g). The enhanced source of moisture to cloud base, along with weakened entrainment of dry FT
314 air, prevents the cloud from thinning to the same extent. Although the change in LWP is only 2–3 g m^{−2}, this amounts to a 10%
315 increase, which helps drive a strong negative SDE at midday and early afternoon.



316

317 **Figure 5.** 3-day timeseries showing the initial domain averaged cloud response to a layer of absorbing aerosol in the base
 318 experiment. In the first column the black dashed lines refer to the control experiment (no-aerosol) and solid blue lines to the
 319 experiments with the aerosol layer present. The second column shows the cloud response (red solid line). The plots show a) the
 320 altitude of the cloud base and top, b) the entrainment rate w_e , c) the liquid water path (LWP), d) the mean relative humidity (RH)
 321 below cloud base, e) the surface latent heat flux (LHF), f) the total mass of water in the boundary layer (BL) column, g) the mean
 322 squared BL vertical velocity perturbation ($w'w'$), and h) the semi-direct effect.



323

324 The analysis of the initial cloud response shows that the first two days are characterised by a general thickening of the cloud
325 driven by the reduction in w_e across the temperature inversion and subsequent enhanced RH profile below cloud. The weakened
326 w_e , BL dynamics, and moisture flux from the surface begin to dry the BL resulting in less cloud growth overnight, whilst the
327 lower cloud base enhances coupling to the surface moisture fluxes during the middle of the day, and less cloud decay.

328

329 3.2.2 Steady-state response in the base experiment

330 The final three days of the 15-day base experiment provide a mean diurnal cycle of the cloud response. The steady-state
331 response of the cloud to the elevated aerosol layer, shown in Fig. 6, shows strong similarities to the third day of the initial
332 response: the growth phase of the cloud (Fig. 6b) is weakened, producing a thinner cloud in the morning, and the decay phase
333 of the cloud (Fig. 6b) is weakened, producing a thicker cloud in the early afternoon. This modification to the diurnal cycle of
334 the cloud is driven by an increased coupling between surface moisture flux and cloud base during the daytime and an overall
335 decrease in total water content and weakened dynamics overnight. The decrease in cloud layer height allows better mixing
336 beneath the cloud base, which enhances the evaporation of moisture from the surface between 0900 and 1500 (Fig. 6d); this is
337 evident from the lack of a diurnal cycle in below-cloud RH (Fig. 6c), which usually occurs due to poor mixing, and the
338 strengthened BL dynamics at midday (Fig. 6f).

339

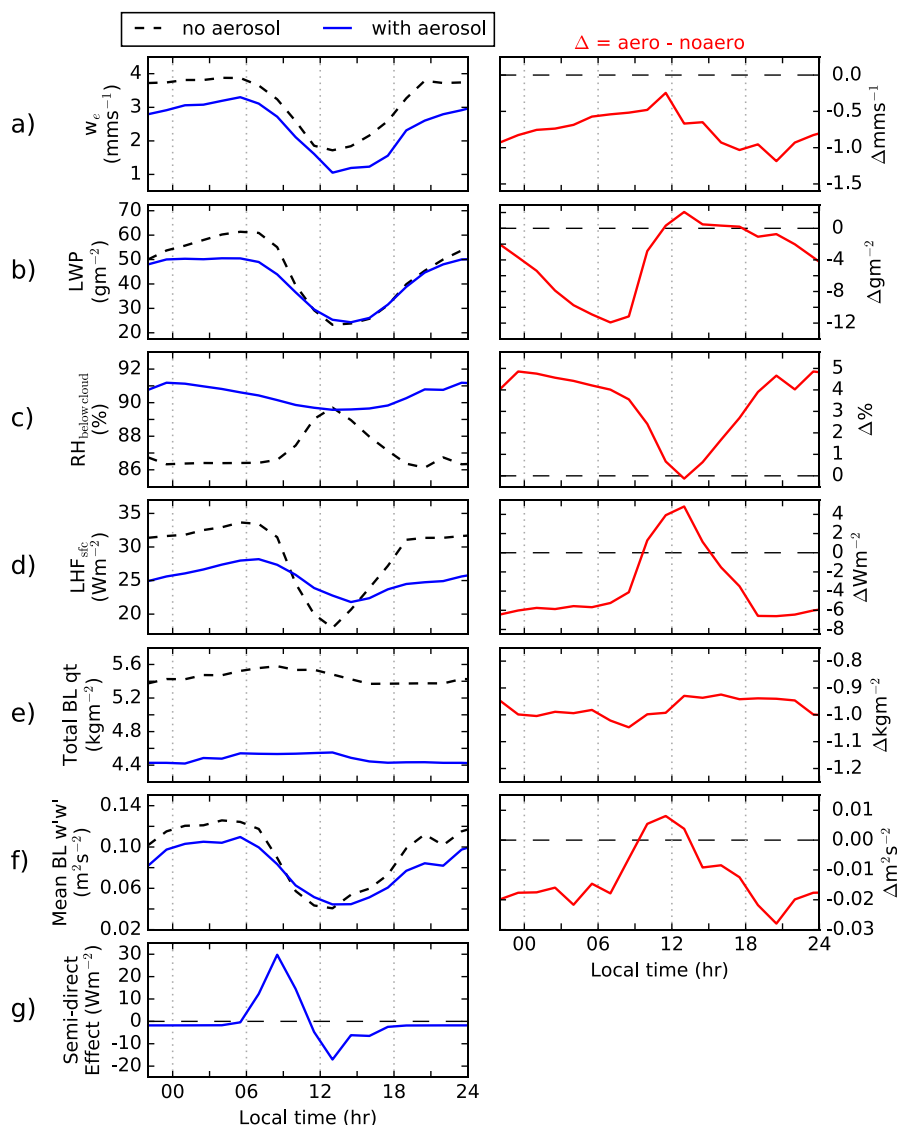
340 The weakened cloud growth phase overnight occurs due to a 15% reduction in total water content of the BL (Fig. 6e) and a
341 reduction in mean BL vertical motions overnight of $\sim 20\%$, indicated by the mean perturbation to vertical velocity in the BL
342 ($w'w'$) in Fig. 6f. The reduction in w_e (Fig. 6a) and subsequent changes to below-cloud water vapour set up a positive feedback
343 mechanism with BL dynamics: vertical motions in the BL are considerably weakened throughout the night and slightly
344 strengthened at midday. Although there is a decrease in LWP there is no systematic impact to the cloud-top longwave cooling
345 due to its weak sensitivity to LWP above 50 g m^{-2} (van der Dussen et al., 2013; Garrett and Zhao, 2006). The weakened BL
346 circulation is therefore due to a reduction in evaporation and associated cooling of entrained air, which weakens cloud-top
347 buoyancy production. These combined changes result in reduced vertical motions within the BL, which reduce surface
348 evaporation, cloud LWP, and buoyancy production from condensation at cloud base, which allow the reduced vertical motions
349 to persist. A partial offset to this process occurs during midday when stronger coupling to the surface results in enhanced
350 transport of water vapour to the cloud base.

351

352 The steady-state response establishes itself by the third day of the simulation. The daily mean steady-state SDE (Fig. 6g)
353 results from a balance between the degree to which the BL total column water content has decreased, producing a positive
354 SDE in the morning, and the degree to which the midday coupling is enhanced, producing a negative SDE in the afternoon. In
355 both cases modifications to BL depth, and thus w_e , play a significant role in cloud response and SDE.



356



357

358 **Figure 6. Domain averaged cloud response to a layer of absorbing aerosol directly above the inversion in the base experiment (0 m**
 359 **cloud–aerosol gap, 250-m thick layer, and AOD of 0.2) for the mean diurnal cycle using the final three days of the 15–day simulation.**
 360 **In the first column the black dashed lines refer to the control experiment (no–aerosol) and solid blue lines to the experiments with**
 361 **the aerosol layer present. The second column shows the cloud response (red solid line). The plots show a) the entrainment rate w_e ,**
 362 **b) the liquid water path (LWP), c) the mean relative humidity (RH) below cloud base, d) the latent heat flux (LHF) from the surface,**
 363 **e) the total mass of water (vapour + liquid) in the boundary layer (BL) column, f) the mean squared BL vertical velocity perturbation**
 364 **($w'w'$), and g) the semi–direct effect.**

365



366 3.3 Sensitivity of initial response to aerosol layer properties

367 Figure 7 shows timeseries for the aerosol layer–sensitivity experiments. In this analysis the inversion strength $\Delta\theta_1$ is determined
368 between altitudes z_{upper} and z_{lower} defined as:

369

$$\begin{cases} z_{\text{lower}} = z \text{ at } 0.025 \cdot z_{\text{max}} & \text{below } z_{\text{max}} \\ z_{\text{upper}} = z \text{ at } 0.25 \cdot z_{\text{max}} & \text{above } z_{\text{max}} \end{cases} \quad (3)$$

370

371 where z_{max} is the altitude at which the maximum gradient in θ_1 occurs. The upper value is determined at a lower threshold to
372 limit spurious values occurring from aerosol layers close to the inversion layer that impact θ_1 .

373 3.3.1 Cloud response

374 The majority of experiments show a positive spike in SDE (Fig. 7d, i and n) just after midday on the first day. This occurs due
375 to the lag–time in response between the impact on cloud top height, which is driven by w_e , and the cloud base, which is driven
376 by changes in sub–cloud RH. This lag occurs due to weaker coupling of the cloud and sub–cloud layers and therefore poorer
377 BL mixing around midday (see Fig. 3). This small decrease in LWP and subsequent positive SDE is consistent throughout the
378 range of experiments but mitigated in some cases due to rapid impacts on the LWP (i.e., the 50 m thickness experiment) that
379 occur before BL coupling weakens. This result suggests the specific timing of the incoming aerosol plume may play a role in
380 the cloud response and SDE on the first day.

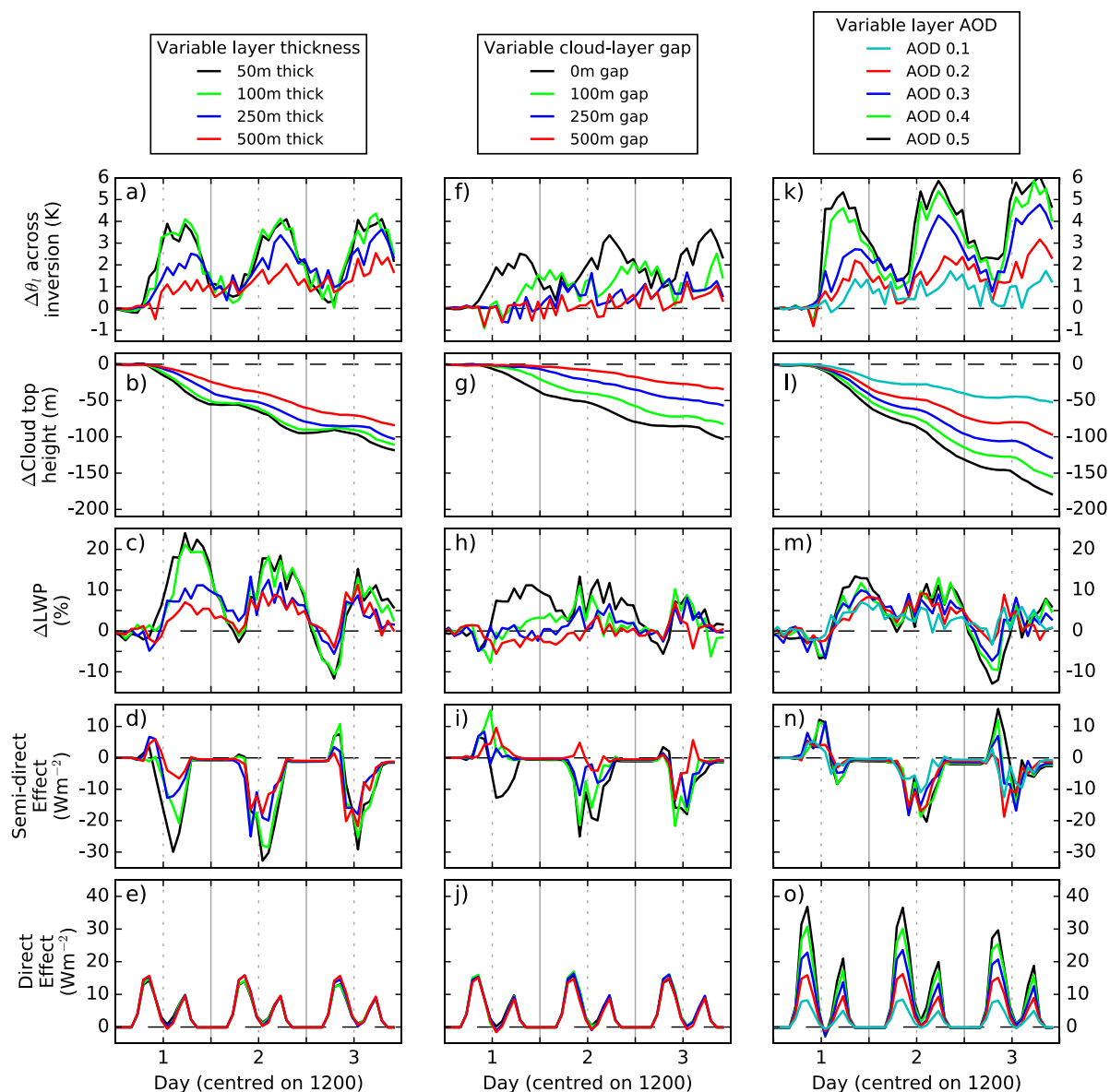
381

382 Geometrically thinner aerosol layers equate, for a given AOD, to a greater aerosol mass mixing ratio and therefore stronger
383 heating. This results in a stronger inversion layer (Fig. 7a) and stronger modification to the LWP response (Fig. 7c) and SDE
384 (Fig. 7d), especially on the first day. This produces a stronger inversion layer, weaker w_e , and a decrease in BL depth (Fig. 7b).
385 For the two thinnest layers the cloud top height decreases at a faster rate during the day than at night, which correlates with
386 the peak heat perturbation. For thicker layers the heat perturbation extends further into the night; this corresponds with the
387 delay in time for the heating towards the top of the layer to reach the inversion layer and drives a steadier reduction in BL
388 depth when compared to the thinner layers. By the third day the BL has started to adjust and less dependence on aerosol layer
389 thickness is apparent, however the thinner layers cause the BL to dry out at a quicker rate, thus producing a stronger positive
390 SDE on the morning of the third day.

391



392



393

394 **Figure 7. 3-day timeseries showing the sensitivity of the initial cloud response to the properties of the elevated absorbing aerosol**
 395 **layer. The three columns correspond to experiments where systematic changes have been made to the aerosol layer thickness (a –**
 396 **e), cloud–aerosol gap (f – j), and aerosol layer AOD (k – o).**

397

398 Increasing the cloud–aerosol gap leads to a weaker and increasingly delayed maximum cloud top height (Fig. 7g) and LWP
 399 response (Fig. 7h) driven by changes in peak strengthening of the inversion (Fig. 7f); this is most pronounced in the first two
 400 days. Only aerosol layers directly above the inversion trigger a considerable cloud response on the first day because of the



401 relatively rapid strengthening of the inversion layer and weakening of w_e which forces the cloud top downwards more rapidly
402 than the RH profile can adjust, resulting in a deeper cloud base. On the second day a cloud response is seen with gaps up to
403 100 m and by the third day all gaps lead to a response in cloud LWP. The delay in response is driven by the delay in the
404 inversion layer strengthening. In the free troposphere the advection of the heat perturbation is driven by subsidence, therefore,
405 greater cloud–aerosol gaps require more time for the heat perturbation to reach the cloud top. Simultaneously longwave cooling
406 acts to weaken the heat perturbation throughout its advection, which drives a relatively weaker strengthening of the temperature
407 inversion as the cloud–aerosol gap increases.

408
409 The initial cloud top response (Fig. 7l) displays a strong dependence on the AOD of the aerosol layer throughout the three days
410 with greater AOD resulting in a greater response. As with geometric layer thickness, larger AODs absorb more radiation and
411 drive a stronger heat perturbation and inversion strength (Fig. 7k). So larger AODs result in a thicker cloud and a more negative
412 SDE. On the third day layers with the largest AODs, which have had the greatest impact on cloud top height and w_e , exhibit a
413 considerably thinner cloud, driving an increasingly positive SDE in the morning.

414
415 In summary, the layer–sensitivity experiments show that on the first day the initial response is for the cloud top to drop quicker
416 than the cloud base, resulting in a thinner cloud and a positive SDE in the morning, the magnitude of which is primarily driven
417 by the proximity of the aerosol layer with the cloud top. With no gap between the inversion at cloud top and aerosol layer, the
418 afternoon of the first day is characterised by a thicker cloud and negative SDE which increases in magnitude for stronger heat
419 perturbations. The second day is generally characterised by an increase in the LWP at midday which drives a negative SDE
420 and is dependent on the location and properties of the aerosol layer. By the third day a consistent pattern occurs: the cloud is
421 consistently thinner in the morning and thicker at midday, the magnitude of which is dependent on the strength of the
422 perturbation.

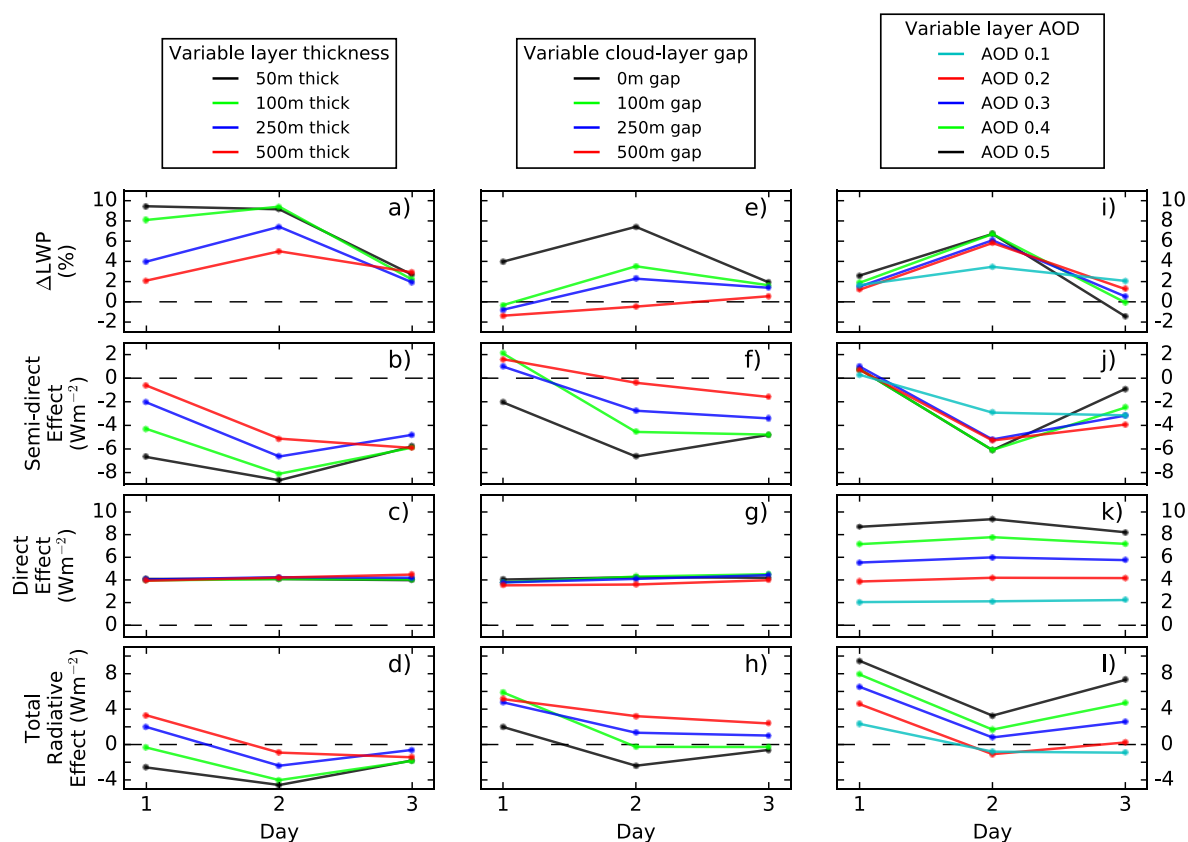
423 3.3.2 Radiative response

424 Figure 8 shows timeseries of the daily mean radiative effects for the layer–sensitivity experiments. The immediate radiative
425 response following the introduction of the absorbing aerosol layer is primarily dependent on the distance between the inversion
426 layer and aerosol layer base. When there is no cloud–aerosol gap the increase in LWP results in a negative SDE; thinner layers
427 and larger AODs increase the inversion layer strengthening and drive a stronger negative SDE on the first day. When any
428 cloud–aerosol gap is present there is little LWP response on the first day due to the delayed inversion layer strengthening,
429 however, all experiments with a gap present are characterised by a small positive SDE. For the experiments with a 50-m gap
430 (variable AOD experiments) the delay is short enough that there is an increase in LWP in the evening of the first day (Fig. 8i).

431
432 On the second and third day the SDE is negative for all experiments; the magnitude of the SDE increases for thinner layers,
433 closer to the inversion layer. When a cloud–aerosol gap is present the AOD tends to have little impact on the magnitude of the



434 SDE. The rate at which the BL moisture content decreases, itself a factor of how strongly w_e is perturbed, results in variations
 435 in which day the peak SDE occurs. In experiments with gaps smaller than 100 m the maximum SDE is reached on the second
 436 day, whereas for gaps larger than or equal to 100 m the maximum occurs on the third day. In all experiments the third day is
 437 characterised by a decrease in the daily mean LWP response which is primarily driven by less cloud growth overnight and in
 438 the morning (see Fig. 7c, h and m) and becomes more pronounced as the temperature inversion strengthens. The thinner cloud
 439 in the morning helps to shift the daily mean SDE towards zero.
 440



441
 442 **Figure 8. Daily mean radiative impact to the elevated aerosol layer properties over the initial three days following the introduction**
 443 **of the aerosol layer for systematic changes to a) – d) aerosol layer thickness, e) – h) cloud–aerosol gap, and i) – l) aerosol optical**
 444 **depth of layer.**

445
 446 The properties of the aerosol layer have a considerable impact on the total radiative effect, calculated as the sum of the DRE
 447 and SDE (Fig. 8d, h, and l). Generally, the SDE acts to counteract the positive DRE and in some cases results in an overall
 448 negative total radiative effect. In all experiments the total radiative effect is sensitive to the layer properties, whereas DRE is
 449 only sensitive to the layer AOD. In many instances the SDE is greater in magnitude than the DRE, with the second day
 450 constituting the period of time with the greatest impact. The relative insensitivity of the SDE to changes in AOD suggest that



451 layers with a moderate AOD (~ 0.2) may have the strongest overall radiative impact due to the relatively low DRE; however,
 452 the behaviour may change for increasing gaps.

453

454 The results of the experiments are summarised in Table 3 with the daily mean SDE alongside the means for the periods before
 455 and after midday. The daily mean SDE is only consistently negative throughout the three days when there is no cloud–aerosol
 456 gap. This result is consistent with Johnson et al. (2004) who similarly found a negative SDE for a ~ 1000 m layer of absorbing
 457 aerosol (AOD of 0.2, SSA of 0.88) directly above the inversion layer. Johnson et al. (2004) calculated a mean SDE of -9.5 Wm^{-2}
 458 and a mean DRE of 10 Wm^{-2} . These magnitudes are greater than in this study but similarly show the SDE is of approximately
 459 equal magnitude to the DRE and of opposite signs. Our results also show that geometrically thin, but optically thick, aerosol
 460 layers will have a stronger forcing than a thicker layer with the same AOD due to a stronger localised heat perturbation; this
 461 effect is most prominent on the first day. When a gap to the aerosol layer base is present our results show that the short–term
 462 SDE is likely to be positive but then becomes negative once the BL has been mixed, which usually occurs during the first night
 463 when BL mixing occurs, highlighting a sensitivity to the specific arrival timing of the incoming plume. On the second and
 464 third day the magnitude of the SDE then depends on the AOD, cloud–aerosol gap, and aerosol layer thickness.

465

466 **Table 3. Mean semi–direct effect (in Wm^{-2}) for each of the aerosol experiments shown in Fig. 2 and Table 2. Mean values are**
 467 **presented for each day (Daily), between 0000 and 1200 hours (am), and between 1200 and 2400 (pm). For the daily mean,**
 468 **increasingly negative values are shaded in blue and increasingly positive in red.**

Type of experiment	gap	dz	AOD	Day 1			Day 2			Day 3		
				Daily	am	pm	Daily	am	pm	Daily	am	pm
Variable gap	0	250	0.2	-2	1	-5	-7	-6	-7	-5	-4	-6
	100	250	0.2	2	4	0	-5	-5	-4	-5	-5	-5
	250	250	0.2	1	2	0	-3	-3	-3	-3	-3	-4
	500	250	0.2	2	1	2	0	1	-1	-2	-3	0
Variable thickness	0	50	0.2	-7	-2	-12	-9	-5	-13	-6	-2	-10
	0	100	0.2	-4	-1	-8	-8	-5	-11	-6	-2	-10
	0	250	0.2	-2	1	-5	-7	-6	-7	-5	-4	-6
	0	500	0.2	-1	2	-3	-5	-4	-6	-6	-5	-7
Variable AOD	50	200	0.1	0	2	-1	-3	-3	-3	-3	-2	-4
	50	200	0.2	1	2	0	-5	-5	-6	-4	-4	-4
	50	200	0.3	1	2	0	-5	-5	-5	-3	-1	-5
	50	200	0.4	1	2	-1	-6	-4	-8	-2	0	-5
	50	200	0.5	1	3	-1	-6	-4	-8	-1	3	-5

469



470 Table 3 highlights the diurnal variations in the SDE. The SDE is generally more negative after midday but that contrast varies
471 with aerosol layer properties. Geometrically thin, optically thick layers, directly above the inversion layer display the strongest
472 contrast with the daily mean SDE dominated by the mean after midday. When a gap is present there is less contrast and both
473 time periods are generally representative of the daily mean, until the BL begins to dry out significantly in the high AOD
474 experiments. These results demonstrate that there are often strong diurnal variations in the SDE which are sensitive to the
475 aerosol layer properties and suggest that observations of the SDE made within a small window of time, e.g., those from polar
476 orbiting satellites, may be unrepresentative of the daily mean SDE.

477 3.4 Sensitivity to boundary layer and cloud properties

478 This section investigates the robustness of the results and conclusions from Sect. 3.3. The parameter space considered in this
479 section includes previous LEM studies, such as Hill and Dobbie (2008) and Johnson et al. (2004), and the range of
480 environmental forcings observed within marine stratocumulus regions.

481

482 The first set of sensitivities focus on the model setup and includes no precipitation from the cloud (*noRain*) and an enhanced
483 large-scale advective heat tendency of -0.5 Kday^{-1} (*05cool*).

- 484 • In the *noRain* setup the production of precipitation is switched off. Stratocumulus frequently produce precipitation in
485 the form of drizzle (Leon et al., 2009) yet studies often simplify simulations by focusing on non-precipitating
486 stratocumulus (e.g., Hill and Dobbie, 2008; Johnson et al., 2004). Precipitation redistributes moisture from the cloud
487 layer to the sub-cloud layer, promoting BL stability and acting to reduce BL dynamics and cloud LWP (Ackerman
488 et al., 2009).
- 489 • In the *05cool* sensitivity, the magnitude of the large-scale advective heat tendency is increased from -0.1
490 to -0.5 Kday^{-1} . That parameter accounts for the equatorward transport of the large-scale air mass and is negative in
491 subtropical marine regions. This value can be estimated using large-scale reanalyses (e.g., Johnson et al., 2004) or
492 used as a balancing term to prevent subsidence heating (e.g., Duynkerke et al., 2004) and represents a degree of
493 variability in LES setups.

494

495 The second set of sensitivities focuses on properties of the BL that may impact the diurnal cycle and maintenance of the cloud.

- 496 • In the *SST-1K* and *SST+1K* setups, SST is decreased and increased by 1K, respectively, while keeping the BL depth
497 at 600 m. Stratocumulus decks in the Atlantic and Pacific Oceans are observed over a wide range of sea surface
498 temperatures (Sandu and Stevens, 2011; Wood, 2012). As the SST increases the differential temperature across the
499 surface-air boundary increases, resulting in more pronounced surface moisture and sensible heat fluxes.
- 500 • The *wetFT* setup increases the mass mixing ratio of water vapour in the FT by $+0.4 \text{ g kg}^{-1}$ to assess the impact of the
501 water vapour content of the entrained air on the SDE. Trajectory analyses from the Pacific and Atlantic Oceans by



502 Sandu et al. (2010) show that the mass mixing ratio of water vapour in the FT varies spatially and temporally, ranging
 503 from 1.0 to 7.5 g kg⁻¹ at 700 hPa; this result is supported by in-situ data summarised by Albrecht et al. (1995).
 504 • The 800-m and 1000-m setups increase the height of the temperature inversion by 200 and 400 m, respectively, by
 505 changing the large-scale divergence rate and initial profiles of θ_l and q_t , while keeping SST constant at 287.2 K.
 506 Observations show that cloud top heights in regions of semi-permanent stratocumulus coverage (southeast Atlantic,
 507 southeast Pacific, and northeast Pacific) typically range from ~500 to ~1500 m (Muhlbauer et al., 2014; Painemal et
 508 al., 2014; Wyant et al., 2010) with variations driven by SST and subsidence.

509
 510 To isolate the cloud response due to the aerosol layer, the cloud-sensitivity experiments are initialised using profiles that
 511 produce an approximately constant stratocumulus cloud layer at the top of the BL following the method described in Sect. 2.2.
 512 Table 4 shows the resulting initial profiles and large-scale divergence rates for each setup. The daily mean SDE on day 2
 513 following the introduction of the absorbing aerosol layer (day 7 of the simulation) is shown in Table 5 for each setup and
 514 aerosol experiment. For the *control* setup the SDE values are the same as shown in Fig. 8.

515
 516 **Table 4. Initial profiles of liquid-water potential temperature (θ_l in K) and total liquid mass-mixing ratio (q_t in g kg⁻¹) against**
 517 **altitude (z in m) for each cloud-sensitivity setup. Values in parentheses indicate the large-scale divergence rate (D in s⁻¹) used for**
 518 **each setup. All setups result in a stable stratocumulus cloud deck at the top of the boundary layer.**

z	<i>noRain</i> (5.4×10^{-6})		<i>05cool</i> (6.2×10^{-6})		<i>SST-1K</i> (4.75×10^{-6})		<i>SST+1K</i> (5.75×10^{-6})		<i>wetFT</i> (5.25×10^{-6})		<i>800m</i> (4.0×10^{-6})			<i>1000m</i> (2.75×10^{-6})		
	θ_l	q_t	θ_l	q_t	θ_l	q_t	θ_l	q_t	θ_l	q_t	z	θ_l	q_t	z	θ_l	q_t
0	287.5	9.0	287.3	9.0	286.5	8.6	288.3	9.4	287.3	9.0	0	287.3	9.0	0	287.3	9.0
600	287.5	9.0	287.3	9.0	286.5	8.6	288.3	9.4	287.3	9.0	800	287.3	9.0	1000	287.3	9.0
601	297.0	5.5	296.0	5.5	296.0	5.5	297.2	5.5	297.0	5.9	801	297.0	5.9	1001	297.0	5.9
750	300.0	5.5	299.0	5.5	300.0	5.5	300.0	5.5	299.5	5.9	900	299.5	5.9	1100	299.5	5.9
1000	301.7	5.5	300.3	5.5	301.7	5.5	301.7	5.5	301.5	5.9	1200	301.5	5.9	1300	301.5	5.9
1500	303.2	5.5	301.5	5.5	303.2	5.5	303.2	5.5	302.6	5.9	1700	302.6	5.9	1900	302.6	5.9
2600	304.0	5.5	302.8	5.5	304.0	5.5	304.0	5.5	303.8	5.9	2600	303.8	5.9	2600	303.8	5.9

519

520 3.4.1 Sensitivity to model setup

521 The removal of precipitation results in stronger BL dynamics and a greater peak in LWP (+15 g m⁻²). Compared to the *control*
 522 setup the *noRain* setup is characterised by a consistent strengthening of the SDE at +1 Wm⁻² when a cloud-aerosol gap is
 523 present and up to +3 Wm⁻² when there is no gap. In the *control* setup the presence of the aerosol layer increases cloud LWP,
 524 which is partially offset by an increase in precipitation. In the *noRain* setup that partial offset is not allowed, resulting in
 525 relatively enhanced LWP response and SDE.



526

527 Increasing the cooling rate of the large-scale advective heat tendency produces stronger buoyancy production and BL
528 dynamics, which are balanced by stronger subsidence ($D = 6.2 \times 10^{-6} \text{ s}^{-1}$) in order to maintain a 600 m BL depth. An enhanced
529 cloud top entrainment of warm dry air is balanced by enhanced flux of vapour from below-cloud and surface LHF. Relative
530 to the *control* setup the aerosol layer has a more pronounced impact on the cloud dynamics and results in a greater decrease in
531 w_e ; this is likely due to the enhanced role that evaporation of entrained air has on buoyancy production in the *05cool* setup.
532 Below-cloud the two setups have a consistent dynamical response, however, in the *05cool* setup the cloud maintenance is
533 more dependent on the below-cloud flux of water vapour. This causes a quicker decrease in BL water content which becomes
534 more pronounced throughout the simulation and manifests as a more pronounced period of positive SDE and a less negative
535 mean SDE on the third day, which in some experiments results in a positive daily mean SDE (not shown).

536 3.4.2 Sensitivity to BL properties

537 In the no-aerosol simulations warmer SST drives an enhanced advection of water vapour below cloud, and a lower LWP due
538 to an increase in BL temperature. The warmer BL also leads to stronger in-cloud buoyancy production. When the aerosol layer
539 is present the LWP response increases with SST, driving a stronger negative SDE in all experiments. The cloud response is
540 particularly sensitive to SST when the aerosol layer is near the cloud top. As discussed in Sect. 3.2, the initial response from
541 the weakened w_e , and subsequently enhanced RH, occurs quicker than the moisture source from the surface can readjust to.
542 The reduction in entrainment rate and BL depth are equivalent for all SST, but the greater flux of moisture from warmer SST
543 results in a greater increase in mean q_t and RH perturbation, leading to a lower cloud base, thicker cloud, and tending to push
544 the SDE towards a more negative daily mean. The sensitivity of the radiative response is driven both by the SST and the
545 perturbation to w_e , therefore stronger heat perturbations closer to the cloud top result in a more pronounced sensitivity to SST.
546

547 The no-aerosol simulation for the *wetFT* setup is characterised by an LWP $+5 \text{ g m}^{-2}$ greater than the *control* setup, with slightly
548 weaker surface evaporation. This increase in LWP is caused by entrainment of slightly moister FT air in the *wetFT* setup,
549 allowing the BL to maintain a greater RH. The mixing of entrained air has a smaller impact on the cloud humidity, which then
550 does not need to be balanced as strongly from a source at the surface. When the aerosol layer is present the weakened w_e
551 therefore has a smaller impact on the RH response of the BL, which results in a smaller SDE. This setup shows that the degree
552 by which the entrained air impacts the cloud plays an important role in the strength of the SDE: very dry FT air will play a
553 more important role in reducing RH, so that a perturbation to w_e will have a greater impact on the cloud response.

554



555 **Table 5. Daily mean semi-direct radiative effect for the second day following the introduction of the absorbing aerosol layer for**
 556 **control and cloud-sensitivity setups. All values are in daily mean Wm^{-2} with increasingly negative values shaded in blue and**
 557 **increasingly positive values shaded in red. Layer properties include the cloud-aerosol gap ('gap', in metres), the geometric thickness**
 558 **of the layer ('dz', in metres), and the aerosol optical depth (AOD) of the layer given at a mid-band wavelength of 505 nm.**

Type of experiment	gap	dz	AOD	control	noRain	05cool	SST-1K	SST+1K	wetFT	800-m	1000-m
Variable gap	0	250	0.2	-7	-8	-5	-5	-8	-6	4	17
	100	250	0.2	-5	-6	-5	-3	-7	-3	6	10
	250	250	0.2	-3	-4	-4	-1	-5	-2	6	6
	500	250	0.2	0	-1	-2	1	0	0	4	2
Variable thickness	0	50	0.2	-9	-12	-7	-7	-13	-8	0	18
	0	100	0.2	-8	-10	-7	-5	-11	-7	2	20
	0	250	0.2	-7	-8	-5	-5	-8	-6	4	17
	0	500	0.2	-5	-7	-5	-2	-8	-5	5	11
Variable AOD	50	200	0.1	-3	-5	-3	-1	-3	-3	6	7
	50	200	0.2	-5	-7	-4	-3	-6	-5	5	15
	50	200	0.3	-5	-9	-4	-4	-8	-6	5	22
	50	200	0.4	-6	-9	-5	-4	-10	-5	6	25
	50	200	0.5	-6	-7	-5	-4	-10	-5	5	26

559

560 3.4.3 Sensitivity to BL depth

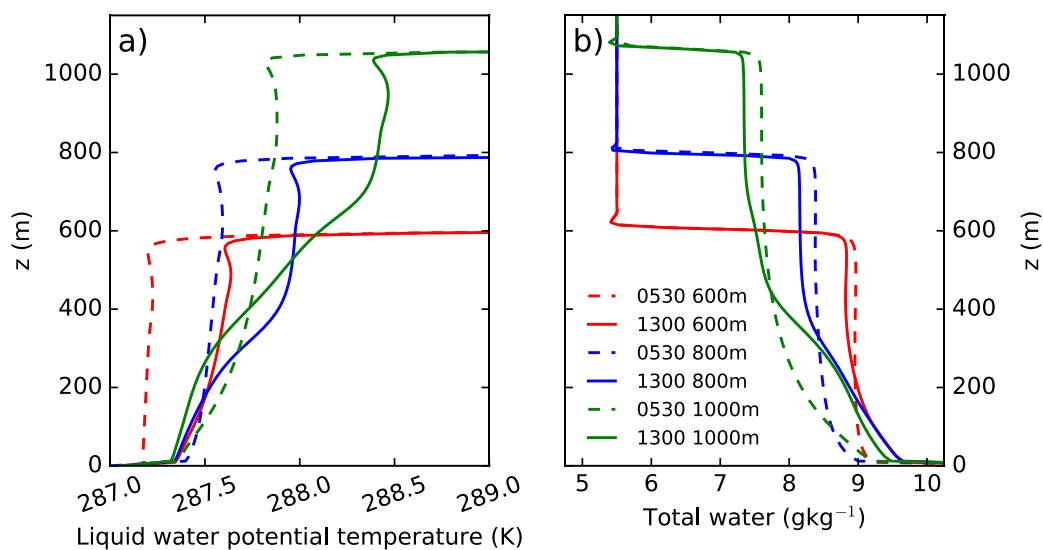
561 As the BL depth increases its temperature increases and the total water content decreases. Figure 9 shows the profiles of θ_1 and
 562 q_1 for the three setups (*control*, *800-m*, *1000-m*) during the time of strongest (0530 hours) and weakest (1300 hours) BL
 563 dynamics. During the period with weakest dynamics the degree of coupling, or mixing, between the sub-cloud and cloud
 564 layers is weakened. This reduces the flux of water vapour from the surface layer to the cloud, and results in a redistribution of
 565 water from the cloud layer to the surface layer (Fig. 9b). That redistribution becomes more pronounced as the BL depth
 566 increases, increasing BL decoupling.

567

568 Increasing the BL depth has a dramatic effect on the sign and magnitude of the SDE shown in Table 5. The SDE switches sign
 569 from negative for a 600-m deep BL in the *control* setup to positive in the *800-m* and *1000-m* setups. The SDE in the *800-m*
 570 setup is roughly of equal magnitude to the *control* but the *1000-m* setup is considerably greater in magnitude, peaking at
 571 $+26 Wm^{-2}$. Responses for the base experiment shown in Fig. 10 help to understand why the BL depth has such a strong impact
 572 on the SDE. In all setups the cloud top height decreases by ~ 100 m over the three days (Fig. 10a, g, and m), driven by similar
 573 changes in w_e (Fig. 10e, k, and q), however the response in cloud base height depends on the simulation and accounts for the
 574 variation in LWP response (Fig. 10b, h, and n). In the *1000-m* setup (Fig. 10m) the cloud base decreases less than the cloud
 575 top throughout the timeseries, driving a consistently reduced LWP.



576



577

578 **Figure 9. Vertical profiles of a) liquid water potential temperature and b) total water mass mixing ratio taken at 0530 (dashed lines)**
579 **and 1300 (solid lines) on day 1 (after spin-up) for the no-aerosol simulations.**

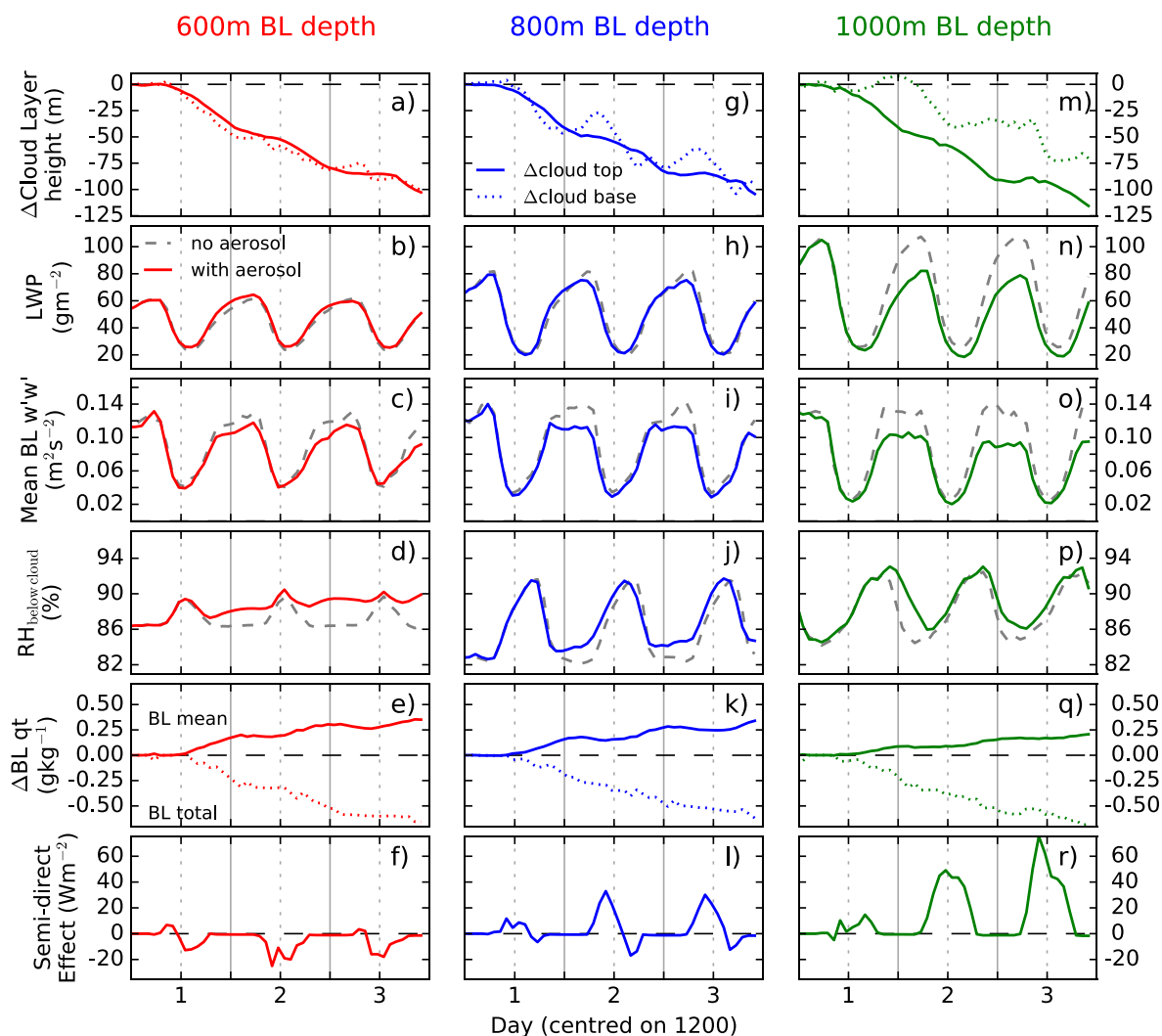
580

581 As shown in Fig. 9 the degree of decoupling between the sub-cloud and cloud layers increases with BL depth. The diurnal
582 cycle of the sub-cloud RH for the three setups (Fig. 10d, j, and p) shows that longer periods of decoupling occur as the BL
583 depth increases (peaks in sub-cloud RH correspond to a poorly mixed BL). In both the *control* and *800-m* setups the BL is
584 reasonably well mixed throughout the day. The presence of the aerosol layer enhances the midday coupling and weakens the
585 cloud decay phase, producing a thicker cloud in the afternoon. However, for the *1000-m* setup the lowering of the cloud layer
586 is not sufficient to overcome the decoupling that occurs, therefore there is no additional flux of moisture at midday and the
587 cloud does not thicken, producing a positive SDE in the afternoon. As the BL deepens overnight, the dynamics become
588 increasingly sensitive to the elevated absorbing aerosol layer (Fig. 10c, i, and o). The result is a more pronounced decrease in
589 the cloud growth phase overnight and a thinner cloud in the morning. The *800-m* and *1000-m* setups produce a strong positive
590 SDE in the morning from day 2 onwards (Fig. 10l and r), which dominates the daily mean SDE (Table 5). As described in
591 Sect. 3.2.2, reductions in w_e and below-cloud moisture fluxes set up a feedback mechanism that decreases the BL dynamics.
592 As the BL deepens this mechanism occurs more rapidly and may be further enhanced by reduced cloud-top longwave cooling
593 that occurs when the LWP is sufficiently reduced. The reduction by $\sim 30 \text{ g m}^{-2}$ of the LWP in the *1000-m* setup is a large
594 enough perturbation to reduce the longwave cloud-top cooling by $\sim 40\%$ and decrease buoyancy production.

595



596



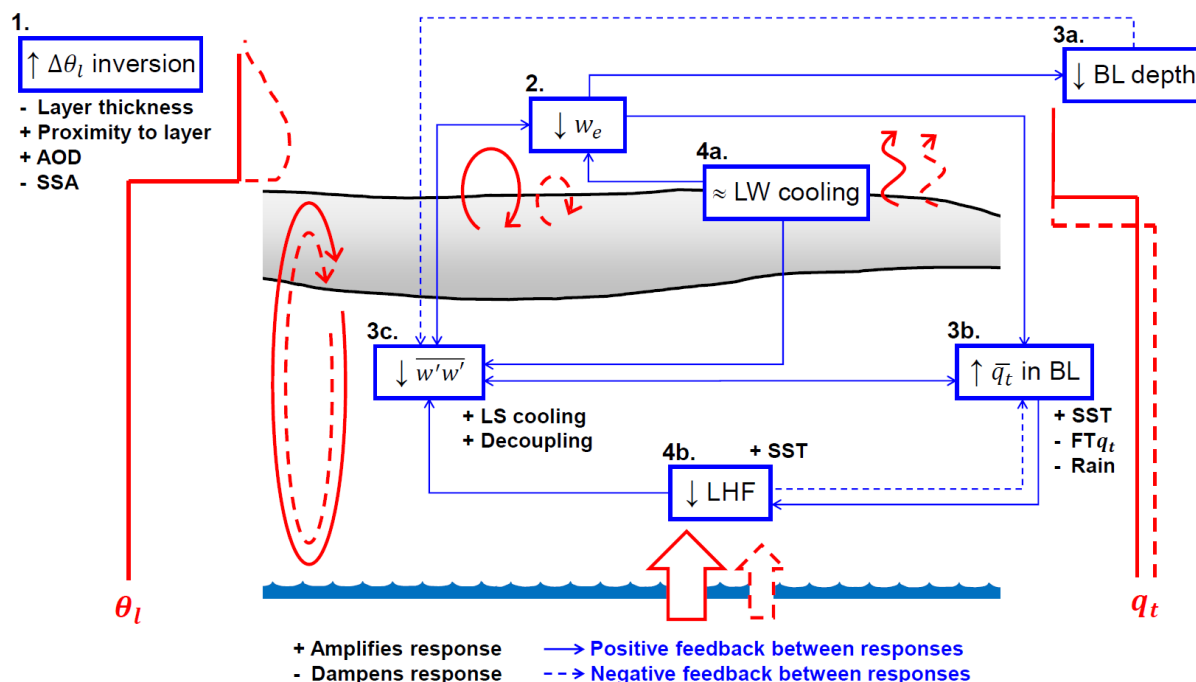
597

598 **Figure 10.** 3-day timeseries showing the initial response of the cloud to a 250 m thick layer of aerosol directly above the inversion
 599 with an aerosol optical depth of 0.2 from the a) – f) control setup with a boundary layer depth of 600 m, g) – l) 800-m setup, and m)
 600 – r) 1000-m setup.

601 These results explain the different aerosol–layer sensitivities shown in Table 5. In all setups the enhanced temperature inversion
 602 weakens w_e and the mixing of warm, dry FT air into the cloud layer and enhances midday coupling. For the *control* setup there
 603 is little impact on BL dynamics, so the cloud becomes thicker due to enhanced sources of moisture; as the temperature inversion
 604 strengthens this response increases. As the BL deepens the BL dynamics are increasingly weakened, driving a reduction in
 605 sub–cloud sources of moisture and a thinner cloud; as the temperature inversion strengthens this response also increases. The
 606 1000-m setup represents an extreme case of this scenario, whereas in the 800-m setup the enhanced coupling is sufficient to
 607 produce an increase in sub–cloud moisture flux during the afternoon, which acts to partially mitigate the cloud thinning.



608 4 Discussion and conclusions



609

610 **Figure 11.** Summary of how the semi-direct effect manifests in a cross section of a stratocumulus-topped boundary layer. Solid red
 611 lines refer to the no-aerosol simulation and dashed red lines to the elevated absorbing aerosol-layer simulations. Key responses to
 612 the boundary layer profiles are depicted in the blue boxes and include the strength of the inversion layer ($\Delta\theta_l$ inversion), entrainment
 613 rate (w_e), boundary layer depth (BL depth), cloud-top longwave cooling (LW cooling), mean vertical motions in the boundary layer
 614 ($\overline{w'w'}$), mean total water content of the BL ($\overline{q_t}$), and the latent heat flux at the ocean surface (LHF). Solid (dashed) arrows between
 615 boxes represent positive (negative) feedbacks between responses. For each response we include properties of the aerosol layer,
 616 boundary layer, or model setup that amplify (denoted by +) or dampen (denoted by -) the response; this includes the aerosol layer
 617 thickness (Layer thickness), cloud-aerosol gap (Proximity to layer), the aerosol optical depth of the layer (AOD), the single scattering
 618 albedo of the aerosol layer (SSA), the sea surface temperature (SST), the water content of the free troposphere (FT q_t), precipitation
 619 (Rain), large-scale advective heat tendency (LS cooling), and the degree of boundary layer decoupling (Decoupling).

620

621 Figure 11 summarises the findings of this study. The SDE manifests itself as a modification to the processes that maintain the
 622 supply of moisture to the cloud layer and are ultimately driven by the strengthened inversion layer and weakened entrainment
 623 rate caused by an absorbing aerosol layer above the inversion. The initial sequence of responses to an elevated layer of
 624 absorbing aerosol is summarised below, with numbers referring to each response labelled in Fig. 11:

- 625 1. The absorbing aerosol layer produces a heat perturbation that results in a strengthened temperature inversion.
- 626 2. Buoyant parcels of air in the BL require more energy in order to push through the strengthened temperature inversion.
 627 This weakens the entrainment rate (w_e) across the inversion layer.
- 628 3a. Weakened entrainment results in a decrease in the cloud top altitude and BL depth.
- 629 3b. The reduction in the entrainment of warm and dry air from the FT reduces the amount of mixing, reducing the sink
 630 of q_t in the cloud layer and allowing the BL to maintain a greater RH. The result is an increase in $\overline{q_t}$ and RH.



- 631 3c. Weakened entrainment reduces the production of buoyancy from evaporative cooling of entrained air, causing a
632 decrease in BL dynamics ($\overline{w'w'}$), especially overnight.
- 633 4a. Cloud–top longwave cooling remains unchanged due to the weak sensitivity to LWPs larger than 50 g m^{-2} overnight
634 and the relatively small changes in LWP during the daytime.
- 635 4b. Increased $\overline{q_t}$ in the BL and weakened BL dynamics reduces the evaporation rate of water from the surface, as
636 evidenced by the reduction in latent heat flux (LHF).

637

638 According to the model sensitivity simulations presented, SDE is increased through the following mechanisms:

- 639 – Geometrically thinner aerosol layers of high aerosol density and low SSA, which produce a stronger localised heat
640 perturbation.
- 641 – Aerosol layers close to the inversion, while larger cloud–aerosol gaps result in a delayed and weaker cloud response.
- 642 – Warmer SSTs, which enhance the flux of moisture to the BL. As a secondary response, the increased SST also drives
643 a stronger reduction in LHF and causes the BL to adjust at a quicker rate.

644 Conversely, SDE is reduced by:

- 645 – Precipitation that, as a sink of cloud liquid water, dampens the cloud response. It follows that any feedbacks that
646 result in an increase in precipitation further weakens the SDE.
- 647 – Increases to the large–scale advective heat tendency (stronger cooling), which are balanced by enhanced buoyancy
648 production from w_e and a more rapid BL adjustment.
- 649 – An increase in the moisture content of the FT, which increases the role that entrainment plays in the supply of moisture
650 to the BL.

651 Finally, an increase in the degree of decoupling in the BL increases the sensitivity of the BL dynamics to changes in w_e , driving
652 towards a positive daily mean SDE. Extreme cases result in a strong positive SDE from day two after applying the aerosol
653 perturbation onwards.

654

655 Several feedbacks between responses occur as the BL adjusts to the perturbations. The key feedbacks occur in the sub–cloud
656 layer and can work together to greatly reduce the supply of moisture to the cloud layer. Processes that act to decrease $\overline{w'w'}$
657 also further decrease w_e and the LHF; these changes weaken the response of $\overline{q_t}$ in the BL so that there is a weaker flux of q_v
658 to the cloud layer. Reduced w_e and a reduction in condensation at the base of the cloud layer weakens buoyancy production in
659 the cloud layer which acts to further decrease $\overline{w'w'}$ and w_e . These feedbacks are most pronounced during the cloud growth
660 phase overnight when the diurnal cycles of w_e , $\overline{w'w'}$, and LHF peak, resulting in a weakened cloud growth phase and a thinner
661 cloud overnight and into the morning when the aerosol layer is present, thus producing a positive SDE. Longwave cloud–top
662 cooling is only weakly sensitive to changes in LWP above 50 gm^{-2} and therefore we do not see changes in the buoyancy



663 production from this process unless the LWP is significantly impacted, which occurs when the BL is decoupled. In this case
664 the reduced LWP further weakens the buoyancy production in the cloud layer, and consequently w_e and BL dynamics.

665

666 A second adjustment feedback on the cloud maintenance occurs through the reduced depth of the BL which acts to promote
667 coupling of the cloud and sub-cloud layers. In this case the feedback mechanism outlined previously acts in reverse so that
668 $\overline{w'w'}$, LHF, and the supply of q_v to the cloud layer increase. This weaker feedback mechanism likely occurs throughout the
669 diurnal cycle but only becomes important at midday when BL dynamics and sub-cloud moisture fluxes are at their weakest
670 and most sensitive to small changes. This adjustment results in reduced cloud decay throughout the afternoon and a thicker
671 cloud, and thus negative SDE, when the elevated layer of absorbing aerosol is present. The strength of this feedback mechanism
672 decreases as the degree of BL decoupling increases until the mechanism ceases to have any impact on the BL; in our study
673 this occurs when the BL is 1000 m deep.

674

675 The sign and magnitude of the SDE from elevated layers of absorbing aerosol is sensitive to the layer properties and BL
676 properties, especially the diurnal variations in coupling between the cloud and sub-cloud layers. For coupled BLs, the SDE on
677 the first day after adding the absorbing aerosol layer is slightly positive unless the aerosol layer is close to the inversion layer.
678 On the second and third day the SDE is strongly negative and peaks on the second day. Generally, for coupled BLs the SDE
679 is of opposite sign to the DRE and often greater in magnitude, resulting in a small or negative total radiative effect for aerosol-
680 radiation interactions from elevated absorbing aerosol layers. For BLs that show characteristics of being decoupled for most
681 of the diurnal cycle the SDE is positive for all three days and increases in magnitude throughout; as the BL becomes more
682 decoupled the magnitude of the SDE increases. For decoupled BLs the SDE acts to enhance the DRE, resulting in a larger total
683 radiative effect.

684

685 The increased LWP and negative SDE in the well-mixed coupled BL experiments is consistent with satellite observations over
686 the southeast Atlantic from Adebisi and Zuidema (2018) and Wilcox (2012). However, our LEM simulations suggest a positive
687 SDE in decoupled BL regions, such as near the stratocumulus-to-cumulus transition region. In reality, the BL may not be as
688 decoupled as in the simulations. The deepening BL is usually accompanied by an increasing SST (Sandu and Stevens, 2011)
689 which was not represented in our simulations; the increase in SST would provide a considerably larger flux of moisture from
690 the surface and enhance the production of buoyancy at the surface which may act to weaken the sensitivity of the BL to changes
691 in dynamics. Contrary to the results presented here, the stratocumulus-to-cumulus transition LES studies by Yamaguchi et al.
692 (2015) and Zhou et al. (2017) suggest that only those elevated smoke layers that are very close, or in direct contact with, the
693 cloud layer impact the cloud properties. However, in these studies the prescribed subsidence rate above the cloud layer was -1.5
694 to -2 mms^{-1} , which is lower than used in our study (-5 mms^{-1} at an equivalent altitude) and would delay the response from the
695 heat perturbation. This difference in subsidence rate represents an important sensitivity to the impact that elevated layers may
696 have on the cloud, both in terms of LES and in the real-world. It is worth noting that Yamaguchi et al. (2015) and Zhou et al.



697 (2017) used the same case study (Sandu and Stevens, 2011) yet found opposing results on whether the absorbing aerosol layer
698 inhibits or hastens the transition to cumulus. Yamaguchi et al. (2015) state that throughout their simulations the BL is decoupled
699 below 800 m, whereas in Zhou et al. (2017) vertical mixing within the BL continues until the inversion height exceeds ~1.4
700 km (Zhou et al., 2017; Fig. 1b). Our results highlight that the cloud response is sensitive to the diurnal variations in BL mixing,
701 which may explain these opposing results.

702

703 Satellite products provide an excellent opportunity to observe aerosol–cloud and aerosol–radiation interactions in remote
704 locations such as the southeast Atlantic Ocean, however most instruments are on polar orbiting satellites that only provide
705 observations from a limited window within the diurnal cycle of the clouds. Our simulations suggest the cloud response to
706 elevated absorbing aerosol layers and the SDE display important diurnal variations so a single observation is unlikely to be
707 representative of the daily mean response. Important changes to the cloud properties occur overnight and play a considerable
708 role in the SDE of the morning period, yet little is known about the impact from absorbing aerosol layers overnight. Future
709 studies should use geostationary satellite observations to investigate the full diurnal cycle of the SDE.

710

711 For a well–mixed coupled BL, the initial cloud and radiative response depend on small–scale processes, such as entrainment
712 and turbulence, which must to be parameterised in climate models. Gordon et al. (2018) used a nested regional model within
713 the Hadley Centre Global Environment Model (HadGEM) to investigate the impact of an incoming elevated plume of smoke
714 in the southeast Atlantic. They found that the elevated aerosol layer reduced cloud top height and enhanced LWP through a
715 reduction in w_e driven by localised heating at or just above the cloud layer of ~6 K. The importance of the weakened w_e aligns
716 well with the LES results of the present study, but the magnitude of the cloud and radiative response are much greater in
717 HadGEM, with an LWP increase of 90%, an increase in cloud fraction of 19% and a mean SDE of -30 Wm^{-2} . Gordon et al.
718 (2018) do not find a consistent longer–term (~3 days) reduction in LWP following BL adjustments. In the LES simulations
719 presented here, cloud fraction remained ~100%, which may be the smaller SDE than Gordon et al. (2018). Additionally,
720 concurrent aerosol–cloud interactions may modify the underlying cloud properties, which may act to amplify the SDE. The
721 lack of BL adjustment may be due to processes that are not explicitly treated in HadGEM, such as BL turbulence and surface
722 fluxes, or due to aerosol–cloud interactions not represented in the LES. Alternatively, differences may be due to different
723 simulated cases. The trajectory analysis of Gordon et al. (2018) suggests that their BL air mass traverses the study region more
724 quickly than the absorbing aerosol layer, which may prevent the BL adjustments from occurring.

725

726 In our simulations the SST and subsidence rate are held constant for the whole duration whereas real stratocumulus decks tend
727 to experience an increasing SST and decreasing subsidence rate. An increasing SST increases surface latent heat fluxes, cloud
728 liquid water content, and the strength of BL eddies, and acts to deepen the BL through increased entrainment and enhance
729 decoupling of the sub–cloud layer (Bretherton and Wyant, 1997). As the cloud is advected over the warmer sea surface the
730 enhanced flux of moisture would act to increase the magnitude of the SDE and prevent the BL from drying out as quickly.



731 Simultaneously, the enhanced decoupling of the sub-cloud layer may result in BL dynamical feedbacks that result in a
732 reduction in LWP (see Fig. 10). Changes to the aerosol distribution within the cloud or in the cloud droplet distribution have
733 not been considered in this study. A weakened w_e increases condensate in the cloud and likely results in an increase in cloud
734 droplet effective radius (r_e). This would promote warm rain process and enhance precipitation, thus reducing the LWP and
735 amplifying the reduction in BL dynamics. These combined effects could lead to a decrease in LWP and shift the SDE towards
736 a positive sign at a quicker rate than suggested by the LES. For the cases where the aerosol layer is directly above the smoke
737 layer an enhanced flux of CCN into the BL would be expected and would act to reduce r_e , suppress precipitation, and act to
738 enhance buoyancy production. The introduction of the absorbing aerosol into the cloud layer would additionally enhance cloud
739 evaporation and act to thin the cloud layer (Hill and Dobbie, 2008; Johnson et al., 2004). Thus, although the experiments where
740 the aerosol layer is directly above the inversion result in the most strongly negative SDE, the response would be at least
741 partially mitigated if the aerosol distribution was represented explicitly. Extending the present study using a binned
742 microphysics scheme would include the additional response of the droplet size distribution and using an aerosol scheme would
743 include the additional impacts the weakened w_e has on the availability of CCN and subsequent cloud response.

744 5 Appendix

745 This appendix describes how the AOD and SSA is prescribed in elevated aerosol layer experiments, along with the geometric
746 thickness of the aerosol layer and the distance between the inversion layer and the aerosol base. In each call to the radiation
747 scheme the desired AOD and SSA are used to determine the mass mixing ratio of two aerosol species, water-soluble like (WS)
748 and biomass-burning like (BB).

749

750 For a single wavelength, the AOD between the altitudes z_0 and z , corresponding to the base and top of the aerosol layer
751 respectively, is calculated as:

$$\text{AOD} = \sum_{i=z_0}^z \sum_{j=WS, BB} (K_{scat_j} + K_{abs_j}) \cdot q_{i,j} \cdot \rho_i \cdot dz_i \quad (\text{A1})$$

752

753 where K_{scat} and K_{abs} are the specific scattering and absorption coefficients, respectively, for the aerosol species j , in units
754 $\text{m}^2 \text{kg}^{-1}$, with mass mixing ratio q in $\text{kg kg}_{\text{dry}}^{-1}$, at each model level i of geometric thickness dz in m, and density of dry air ρ in
755 kg m^{-3} . If the mass mixing ratio of each species is assumed equal and constant with height ($q_{WS} = q_{BB}$ and $q_i = q$), Eq. A1
756 becomes:

757

$$q \cdot \sum_{i=z_0}^z \rho_i \cdot dz_i = \frac{\text{AOD}}{\sum_{j=WS, BB} K_{scat_j} + K_{abs_j}} \quad (\text{A2})$$



758

759 We incorporate a factor X_{SSA} into Eq. A2 that can be used to describe the relative ratio of WS mass to BB mass so that Eq. A2
760 becomes:

$$q \cdot \sum_{i=z_0}^z \rho_i \cdot dz_i = \frac{\text{AOD}}{(K_{scat_{WS}} + K_{abs_{WS}}) + X_{SSA} \cdot (K_{scat_{BB}} + K_{abs_{BB}})} \quad (\text{A3})$$

761

762 Equation A3 can be re-arranged to give q for a given AOD:

763

$$q = \frac{\text{AOD}_{\text{constant}}}{\sum_{i=z_0}^z \rho_i \cdot dz_i} \quad (\text{A4})$$

764 where

$$\text{AOD}_{\text{constant}} = \frac{\text{AOD}}{(K_{scat_{WS}} + K_{abs_{WS}}) + X_{SSA} \cdot (K_{scat_{BB}} + K_{abs_{BB}})} \quad (\text{A5})$$

765

766 Therefore for the two aerosol species:

$$q_j = \begin{cases} q, & j = WS \\ X_{SSA} \cdot q, & j = BB \end{cases} \quad (\text{A6})$$

767

768 The overall SSA is calculated as:

769

$$\text{SSA} = \frac{K_{scat_{WS}} + X_{SSA} \cdot K_{scat_{BB}}}{K_{scat_{WS}} + X_{SSA} \cdot K_{scat_{BB}} + K_{abs_{WS}} + X_{SSA} \cdot K_{abs_{BB}}} \quad (\text{A7})$$

770

771 Equation A7 can be re-arranged to solve for X_{SSA}

772

$$X_{SSA} = \frac{K_{scat_{WS}} - \text{SSA} \cdot (K_{scat_{WS}} + K_{abs_{WS}})}{\text{SSA} \cdot (K_{scat_{BB}} + K_{abs_{BB}}) - K_{scat_{BB}}} \quad (\text{A8})$$

773

774 At the beginning of the simulation X_{SSA} and $\text{AOD}_{\text{constant}}$ are calculated using Equations A8 and A5, respectively, using the
775 shortwave extinction coefficients of the aerosols for the wavelength band 320 – 690 nm and the prescribed AOD and SSA. At
776 each horizontal grid point q is then calculated using Eq. A4 for the elevated aerosol layer where z_0 is the base of the aerosol
777 layer, and z is the top of the aerosol layer. The mass mixing ratio of each species is calculated using Eq. A6 and finally the
778 mass mixing ratio profiles of WS and BB applied to the radiation scheme.



779 6 Author contribution

780 RJH, NB, EJH, and AAH designed the methodology and experiments. AAH provided model expertise and assistance. RJH
781 setup, performed, and post-processed the simulations. RJH, NB, EJH, and AAH analysed the results. RJH provided all
782 visualisations and wrote the initial manuscript draft. NB, EJH, and AAH provided revisions and commentary on the
783 manuscript.

784 7 Competing interests

785 The authors declare that they have no conflict of interest.

786 8 Acknowledgments

787 This research was funded by the UK Natural Environment Research Council (NERC) CLOUDS and Aerosol Radiative Impacts
788 and Forcing: Year 2016 (CLARIFY-2016) project NE/L013479/1. We acknowledge use of the Monsoon system, a
789 collaborative facility supplied under the Joint Weather and Climate Research Programme, a strategic partnership between the
790 Met Office and the Natural Environment Research Council. The CALIOP data were obtained from the NASA Langley
791 Research Center Atmospheric Science Data Center.

792 9 References

793 Ackerman, A. S., vanZanten, M. C., Stevens, B., Savic-Jovicic, V., Bretherton, C. S., Chlond, A., Golaz,
794 J.-C., Jiang, H., Khairoutdinov, M., Krueger, S. K., Lewellen, D. C., Lock, A., Moeng, C.-H., Nakamura,
795 K., Petters, M. D., Snider, J. R., Weinbrecht, S. and Zulauf, M.: Large-Eddy Simulations of a Drizzling,
796 Stratocumulus-Topped Marine Boundary Layer, *Mon. Weather Rev.*, 137(3), 1083–1110,
797 doi:10.1175/2008MWR2582.1, 2009.

798 Adebisi, A. A. and Zuidema, P.: Low cloud cover sensitivity to biomass-burning aerosols and meteorology
799 over the Southeast Atlantic, *J. Clim.*, 31(11), 4329–4346, doi:10.1175/JCLI-D-17-0406.1, 2018.

800 Adebisi, A. A., Zuidema, P. and Abel, S. J.: The convolution of dynamics and moisture with the presence
801 of shortwave absorbing aerosols over the southeast Atlantic, *J. Clim.*, 28(5), 1997–2024,
802 doi:10.1175/JCLI-D-14-00352.1, 2015.

803 Albrecht, B. A., Jensen, M. P. and Syrett, W. J.: Marine boundary layer structure and fractional
804 cloudiness, *J. Geophys. Res.*, 100222(20), 209–14, doi:10.1029/95JD00827, 1995.

805 Bond, T. C., Doherty, S. J., Fahey, D. W., Forster, P. M., Berntsen, T., DeAngelo, B. J., Flanner, M. G.,
806 Ghan, S., Kärcher, B., Koch, D., Kinne, S., Kondo, Y., Quinn, P. K., Sarofim, M. C., Schultz, M. G.,
807 Schulz, M., Venkataraman, C., Zhang, H., Zhang, S., Bellouin, N., Guttikunda, S. K., Hopke, P. K.,
808 Jacobson, M. Z., Kaiser, J. W., Klimont, Z., Lohmann, U., Schwarz, J. P., Shindell, D., Storelvmo, T.,



- 809 Warren, S. G. and Zender, C. S.: Bounding the role of black carbon in the climate system: A scientific
810 assessment, *J. Geophys. Res. Atmos.*, 118(11), 5380–5552, doi:10.1002/jgrd.50171, 2013.
- 811 Bony, S. and Dufresne, J. L.: Marine boundary layer clouds at the heart of tropical cloud feedback
812 uncertainties in climate models, *Geophys. Res. Lett.*, 32(20), 1–4, doi:10.1029/2005GL023851, 2005.
- 813 Boucher, O., Randall, D., Artaxo, P., Bretherton, C., Feingold, G., Forster, P., Kerminen, V.-M., Kondo,
814 Y., Liao, H., Lohmann, U., Rasch, P., Satheesh, S. K., Sherwood, S., Stevens, B. and Zhang, X.-Y.:
815 IPCC AR5 Clouds and Aerosols, in *Climate Change 2013 - The Physical Science Basis*, pp. 571–658,
816 Cambridge University Press, Cambridge, United Kingdom and New York, NY, USA., 2013.
- 817 Bretherton, C. S. and Wyant, M. C.: Moisture Transport, Lower-Tropospheric Stability, and Decoupling
818 of Cloud-Topped Boundary Layers, *J. Atmos. Sci.*, 54(1), 148–167, doi:10.1175/1520-
819 0469(1997)054<0148:MTL TSA>2.0.CO;2, 1997.
- 820 Bretherton, C. S., Blossey, P. N. and Jones, C. R.: Mechanisms of marine low cloud sensitivity to
821 idealized climate perturbations: A single-LES exploration extending the CGILS cases, *J. Adv. Model.*
822 *Earth Syst.*, 5(2), 316–337, doi:10.1002/jame.20019, 2013.
- 823 Chand, D., Wood, R., Anderson, T. L., Satheesh, S. K. and Charlson, R. J.: Satellite-derived direct
824 radiative effect of aerosols dependent on cloud cover, *Nat. Geosci.*, 2(3), 181–184,
825 doi:10.1038/ngeo437, 2009.
- 826 Cook, J. and Highwood, E. J.: Climate response to tropospheric absorbing aerosols in an intermediate
827 general-circulation model, *Q. J. R. Meteorol. Soc.*, 130(596), 175–191, doi:10.1256/qj.03.64, 2004.
- 828 Costantino, L. and Bréon, F. M.: Aerosol indirect effect on warm clouds over South-East Atlantic, from
829 co-located MODIS and CALIPSO observations, *Atmos. Chem. Phys.*, 13(1), 69–88, doi:10.5194/acp-13-
830 69-2013, 2013.
- 831 Das, S., Harshvardhan, H., Bian, H., Chin, M., Curci, G., Protonotariou, A. P., Mielonen, T., Zhang, K.,
832 Wang, H. and Liu, X.: Biomass burning aerosol transport and vertical distribution over the South African-
833 Atlantic region, *J. Geophys. Res.*, 122(12), 6391–6415, doi:10.1002/2016JD026421, 2017.
- 834 van der Dussen, J. J., de Roode, S. R., Ackerman, A. S., Blossey, P. N., Bretherton, C. S., Kurowski, M.
835 J., Lock, A. P., Neggers, R. A. J., Sandu, I. and Siebesma, A. P.: The GASS/EUCLIPSE model
836 intercomparison of the stratocumulus transition as observed during ASTEX: LES results, *J. Adv. Model.*
837 *Earth Syst.*, 5(3), 483–499, doi:10.1002/jame.20033, 2013.
- 838 Edwards, J. M. and Slingo, A.: Studies with a flexible new radiation code. I: Choosing a configuration for
839 a large-scale model, *Q. J. R. Meteorol. Soc.*, 122(531), 689–719, doi:10.1256/smsqj.53106, 1996.
- 840 Feingold, G., Koren, I., Wang, H., Xue, H. and Brewer, W. A.: Precipitation-generated oscillations in open
841 cellular cloud fields, *Nature*, 466(7308), 849–852, doi:10.1038/nature09314, 2010.
- 842 Garrett, T. J. and Zhao, C.: Increased Arctic cloud longwave emissivity associated with pollution from
843 mid-latitudes, *Nature*, 440(7085), 787–789, doi:10.1038/nature04636, 2006.
- 844 Gordon, H., Field, P. R., Abel, S. J., Dalvi, M., Grosvenor, D. P., Hill, A. A., Johnson, B. T., Miltenberger,
845 A. K., Yoshioka, M. and Carslaw, K. S.: Large simulated radiative effects of smoke in the south-east
846 Atlantic, *Atmos. Chem. Phys.*, 18(20), 15261–15289, doi:10.5194/acp-18-15261-2018, 2018.



- 847 Gray, M. E. B., Brown, A. R., Lock, A. P. and Petch, J.: Version 2.3 Of The Met Office Large Eddy Model:
848 Part III. Software Documentation, Met Office, Bracknell, UK. [online] Available from:
849 <http://appconv.metoffice.com/LEM/docs.html>, 2001.
- 850 Hartmann, D. L. and Short, D. A.: On the Use of Earth Radiation Budget Statistics for Studies of Clouds
851 and Climate, *J. Atmos. Sci.*, 37(6), 1233–1250, doi:10.1175/1520-
852 0469(1980)037<1233:OTUOER>2.0.CO;2, 1980.
- 853 Hartmann, D. L., Ockert-Bell, M. E. and Michelsen, M. L.: Hartmann_EtAl_1992_EnergyBalance, *J.*
854 *Clim.*, 5(November), 1281–1304, doi:Doi 10.1175/1520-0442(1992)005<1281:Teocto>2.0.Co;2, 1992.
- 855 Hignett, P.: Observations of Diurnal Variation in a Cloud-capped Marine Boundary Layer, *J. Atmos. Sci.*,
856 48(12), 1474–1482, doi:10.1175/1520-0469(1991)048<1474:OODVIA>2.0.CO;2, 1991.
- 857 Hill, A. A. and Dobbie, S.: The impact of aerosols on non-precipitating marine stratocumulus. II: The
858 semi-direct effect, *Q. J. R. Meteorol. Soc.*, 134(634 A), 1155–1165, doi:10.1002/qj.277, 2008.
- 859 Hill, A. A., Dobbie, S. and Yin, Y.: The impact of aerosols on non-precipitating marine stratocumulus. I:
860 Model description and prediction of the indirect effect, *Q. J. R. Meteorol. Soc.*, 134(634 A), 1143–1154,
861 doi:10.1002/qj.278, 2008.
- 862 Hill, A. A., Feingold, G. and Jiang, H.: The Influence of Entrainment and Mixing Assumption on Aerosol–
863 Cloud Interactions in Marine Stratocumulus, *J. Atmos. Sci.*, 66(5), 1450–1464,
864 doi:10.1175/2008JAS2909.1, 2009.
- 865 Johnson, B. T., Shine, K. P. and Forster, P. M.: The semi-direct aerosol effect: Impact of absorbing
866 aerosols on marine stratocumulus, *Q. J. R. Meteorol. Soc.*, 130(599 PART B), 1407–1422,
867 doi:10.1256/qj.03.61, 2004.
- 868 Klein, S. A., Hall, A., Norris, J. R. and Pincus, R.: Low-Cloud Feedbacks from Cloud-Controlling Factors:
869 A Review, *Surv. Geophys.*, 38(6), 1307–1329, doi:10.1007/s10712-017-9433-3, 2017.
- 870 Koch, D. and Del Genio, A. D.: Black carbon semi-direct effects on cloud cover: review and synthesis,
871 *Atmos. Chem. Phys.*, 10(16), 7685–7696, doi:10.5194/acp-10-7685-2010, 2010.
- 872 Lee, I. Y.: Evaluation of cloud microphysics parameterizations for mesoscale simulations, *Atmos. Res.*,
873 24(1–4), 209–220, doi:[https://doi.org/10.1016/0169-8095\(89\)90046-X](https://doi.org/10.1016/0169-8095(89)90046-X), 1989.
- 874 Leon, D. C., Wang, Z. and Liu, D.: Climatology of drizzle in marine boundary layer clouds based on 1
875 year of data from CloudSat and Cloud-Aerosol Lidar and Infrared Pathfinder Satellite Observations
876 (CALIPSO), *J. Geophys. Res. Atmos.*, 114(8), D00A14, doi:10.1029/2008JD009835, 2009.
- 877 Lu, Z., Liu, X., Zhang, Z., Zhao, C., Meyer, K., Rajapakshe, C., Wu, C., Yang, Z. and Penner, J. E.:
878 Biomass smoke from southern Africa can significantly enhance the brightness of stratocumulus over the
879 southeastern Atlantic Ocean, *Proc. Natl. Acad. Sci.*, 115(12), 2924–2929,
880 doi:10.1073/pnas.1713703115, 2018.
- 881 Monin, A. S. and Obukhov, A. M.: Basic laws of turbulent mixing in the surface layer of the atmosphere,
882 *Geophys. Dir. AF Cambridge Res. Cent.*, 24(151), 163–187, doi:10.1016/j.jallcom.2004.05.088, 1954.
- 883 Muhlbauer, A., McCoy, I. L. and Wood, R.: Climatology of stratocumulus cloud morphologies:



- 884 Microphysical properties and radiative effects, *Atmos. Chem. Phys.*, 14(13), 6695–6716,
885 doi:10.5194/acp-14-6695-2014, 2014.
- 886 Painemal, D., Kato, S. and Minnis, P.: Boundary layer regulation in the southeast Atlantic cloud
887 microphysics during the biomass burning season as seen by the A-train satellite constellation, *J.*
888 *Geophys. Res.*, 119(19), 11,288–11,302, doi:10.1002/2014JD022182, 2014.
- 889 Peers, F., Bellouin, N., Waquet, F., Ducos, F., Goloub, P., Mollard, J., Myhre, G., Skeie, R. B., Takemura,
890 T., Tanré, D., Thieuleux, F. and Zhang, K.: Comparison of aerosol optical properties above clouds
891 between POLDER and AeroCom models over the South East Atlantic Ocean during the fire season,
892 *Geophys. Res. Lett.*, 43(8), 3991–4000, doi:10.1002/2016GL068222, 2016.
- 893 Penner, J. E., Zhang, S. Y. and Chuang, C. C.: Soot and smoke aerosol may not warm climate, *J.*
894 *Geophys. Res. Atmos.*, 108(D21), doi:10.1029/2003JD003409, 2003.
- 895 Rajapakshe, C., Zhang, Z., Yorks, J. E., Yu, H., Tan, Q., Meyer, K., Platnick, S. and Winker, D. M.:
896 Seasonally transported aerosol layers over southeast Atlantic are closer to underlying clouds than
897 previously reported, *Geophys. Res. Lett.*, 44(11), 5818–5825, doi:10.1002/2017GL073559, 2017.
- 898 De Roode, S. R., Siebesma, A. P., Gesso, S. D., Jonker, H. J. J., Schalkwijk, J. and Sival, J.: A mixed-
899 layer model study of the stratocumulus response to changes in large-scale conditions, *J. Adv. Model.*
900 *Earth Syst.*, 6(4), 1256–1270, doi:10.1002/2014MS000347, 2014.
- 901 Sakaeda, N., Wood, R. and Rasch, P. J.: Direct and semidirect aerosol effects of southern African
902 biomass burning aerosol, *J. Geophys. Res.*, 116(D12), D12205, doi:10.1029/2010JD015540, 2011.
- 903 Sandu, I. and Stevens, B.: On the Factors Modulating the Stratocumulus to Cumulus Transitions, *J.*
904 *Atmos. Sci.*, 68(9), 1865–1881, doi:10.1175/2011JAS3614.1, 2011.
- 905 Sandu, I., Stevens, B. and Pincus, R.: On the transitions in marine boundary layer cloudiness, *Atmos.*
906 *Chem. Phys.*, 10(5), 2377–2391, doi:10.5194/acp-10-2377-2010, 2010.
- 907 Sherwood, S. C., Bony, S., Boucher, O., Bretherton, C., Forster, P. M., Gregory, J. M., Stevens, B.,
908 Sherwood, S. C., Bony, S., Boucher, O., Bretherton, C., Forster, P. M., Gregory, J. M. and Stevens, B.:
909 Adjustments in the Forcing-Feedback Framework for Understanding Climate Change, *Bull. Am.*
910 *Meteorol. Soc.*, 96(2), 217–228, doi:10.1175/BAMS-D-13-00167.1, 2015.
- 911 Stjern, C. W., Samset, B. H., Myhre, G., Forster, P. M., Hodnebrog, Ø., Andrews, T., Boucher, O.,
912 Faluvegi, G., Iversen, T., Kasoar, M., Kharin, V., Kirkevåg, A., Lamarque, J. F., Olivíé, D., Richardson,
913 T., Shawki, D., Shindell, D., Smith, C. J., Takemura, T. and Voulgarakis, A.: Rapid Adjustments Cause
914 Weak Surface Temperature Response to Increased Black Carbon Concentrations, *J. Geophys. Res.*
915 *Atmos.*, 122(21), 11,462–11,481, doi:10.1002/2017JD027326, 2017.
- 916 Wilcox, E. M.: Stratocumulus cloud thickening beneath layers of absorbing smoke aerosol, *Atmos.*
917 *Chem. Phys.*, 10(23), 11769–11777, doi:10.5194/acp-10-11769-2010, 2010.
- 918 Wilcox, E. M.: Direct and semi-direct radiative forcing of smoke aerosols over clouds, *Atmos. Chem.*
919 *Phys.*, 12(1), 139–149, doi:10.5194/acp-12-139-2012, 2012.
- 920 Wood, R.: Stratocumulus Clouds, *Mon. Weather Rev.*, 140(8), 2373–2423, doi:10.1175/MWR-D-11-
921 00121.1, 2012.



- 922 Wyant, M. C., Wood, R., Bretherton, C. S., Mechoso, C. R., Bacmeister, J., Balmaseda, M. A., Barrett,
923 B., Codron, F., Earnshaw, P., Fast, J., Hannay, C., Kaiser, J. W., Kitagawa, H., Klein, S. A., Köhler, M.,
924 Manganello, J., Pan, H. L., Sun, F., Wang, S. and Wang, Y.: The PreVOCA experiment: Modeling the
925 lower troposphere in the Southeast Pacific, *Atmos. Chem. Phys.*, 10(10), 4757–4774, doi:10.5194/acp-
926 10-4757-2010, 2010.
- 927 Yamaguchi, T., Feingold, G., Kazil, J. and McComiskey, A.: Stratocumulus to cumulus transition in the
928 presence of elevated smoke layers, *Geophys. Res. Lett.*, 42(23), 10478–10485,
929 doi:10.1002/2015GL066544, 2015.
- 930 Zhang, Y., Stevens, B., Medeiros, B. and Ghil, M.: Low-cloud fraction, lower-tropospheric stability, and
931 large-scale divergence, *J. Clim.*, 22(18), 4827–4844, doi:10.1175/2009JCLI2891.1, 2009.
- 932 Zhou, X., Ackerman, A. S., Fridlind, A. M., Wood, R. and Kollias, P.: Impacts of solar-absorbing aerosol
933 layers on the transition of stratocumulus to trade cumulus clouds, *Atmos. Chem. Phys.*, 17(20), 12725–
934 12742, doi:10.5194/acp-17-12725-2017, 2017.
- 935